An intracontinental orogen exhumed by basement-slice imbrication in the Longmenshan Thrust Belt of the Eastern Tibetan Plateau

Zhenhua Xue, Wei Lin, Yang Chu, Michel Faure, Yan Chen, Wenbin Ji, Huaning Qiu

1 **An intracontinental orogen exhumed by basement-slice-imbrication in the**
2 **Longmenshan Thrust Belt of the Eastern Tibetan Plateau**
3

4 **Zhenhua Xue[1,2,3], Wei Lin[2, 4], Yang Chu[2, 4], Michel Faure[3], Yan Chen[3], Wenbin Ji[5],**
5 **Huaning Qiu[6]**
6 [1] School of Earth Sciences, China University of Geosciences, Wuhan 430074, China
7 [2] State Key Laboratory of Lithospheric Evolution, Institute of Geology and Geophysics,
8 Chinese Academy of Sciences, Beijing 100029, China
9 [3] Univ. Orléans, CNRS, BRGM, ISTO, UMR 7327, F–45071, Orléans, France
10 [4] University of Chinese Academy of Sciences, Beijing 100049, China
11 [5] Department of Geology, Northwest University, Xi'an 710069, China
12 [6] Key Laboratory of Tectonics and Petroleum Resources (China University of
13 Geosciences), Ministry of Education, Wuhan 430074, China
14 Corresponding author: Wei Lin (linwei@mail.iggcas.ac.cn)
15

16 **Key Points**
17 1. The double-vergent structure of the Longmenshan belt was established during the
18 late Triassic intracontinental underthrusting
19 2. Boundary faults of the NW-normal faulting and SE-thrusting facilitated the SE-ward
20 basement-slice imbrication
21 3. The episodic basement-slice imbrication exhumed the early Mesozoic metamorphic
22 rocks
23

24 **Abstract** The Longmenshan Thrust Belt (LMTB) in the Eastern Tibet resulted from a
25 Mesozoic orogeny and Cenozoic reworking. It is generally believed that the Cenozoic
26 tectonics along the LMTB are mostly inherited from the Mesozoic one. Reconstruct the
27 Mesozoic tectonics of the LMTB is therefore important for understanding its
28 evolutionary history. On the basis of detailed structural analysis, we recognized a Main
29 Central Boundary that divides the LMTB into a Southeastern Zone and a Northwestern
30 Zone. Both zones underwent a main D_1 event characterized by the D_{1E} top-to-the-SE
31 thrusting in the Southeastern Zone and the D_{1W} top-to-the-NW/N thrusting in the
32 Northwestern Zone. In the Southeastern Zone, a D_2 top-to-the-NW/N normal faulting

that cuts the D_{1E} structures is developed along the NW boundary of the basement complexes. Newly obtained and previous geochronological data indicate that the D_{1E} and D_{1W} event occurred synchronously at *ca*. 224–219 Ma, and the D_2 top-to-the-NW/N normal faulting was episodically activated at *ca*. 166–160 Ma, 141–120 Ma, 81–47 Ma and 27–25 Ma. Episodically and synchronously activated top-to-the-NW normal faulting and top-to-the-SE thrusting along the northwest and southeast boundary of the basement complexes, respectively, let us propose that the basement-slices were episodically imbricated to the SE during the late Jurassic–early Cretaceous and late Cretaceous–earliest Paleocene. The D_1 amphibolite-facies metamorphic rocks above the basement complexes recorded fast exhumation during the late Jurassic–early Cretaceous. We propose that the early Mesozoic northwestward basement underthrusting along a crustal "weak zone" was responsible for the D_1 double-vergent thrusting and amphibolite-facies metamorphism. Subsequent basement-slice imbrications reworked the LMTB and exhumed the amphibolite-facies rocks. Our results highlight the importance of basement underthrusting and imbrication in the formation and reworking of the intracontinental Longmenshan Thrust Belt in the Eastern Tibet.

1. Introduction

The Longmenshan Thrust Belt (LMTB; Figure 1a), at the eastern margin of the Tibetan Plateau, has attracted attentions of geologists due to the paradox between low convergence rate (Zhang et al., 2004; Shen et al., 2009) and extremely high topographic gradient (Clark and Royden, 2000; Royden et al., 2008) as well as intense seismic activities (e.g., 2008 Wenchuan Mw 7.9 earthquake, 2013 Lushan Mw 7.0 earthquake, and 2017 Jiuzhaigou Mw 7.0 earthquake). This paradox has spawned a vigorous debate regarding the roles of upper crustal faulting (Hubbard and Shaw, 2009) and lower crust channel flow (Royden et al., 2008) in building and maintaining such a high Tibetan Plateau margin. However, both models attribute shortening and crustal thickening of the LMTB to the late Cenozoic evolution, and underestimate the importance of widely recognized Mesozoic tectonics along the LMTB (Xu et al., 1992; Burchfiel et al., 1995; Worley and Wilson, 1996). Furthermore, it has been reached a consensus that the LMTB is mainly inherited from the Mesozoic tectonic framework (Burchfiel et al.,

65   1995; Meng et al., 2005). Elucidating the Mesozoic tectonics of the LMTB and its

66   adjacent areas is therefore crucial to understand the tectonic evolution of the LMTB.

67   The prominent deformation recorded in the LMTB and adjacent areas is indicated

68   by observations including: 1) the peripheral foreland basin formed due to the

69   southeastward thrusting and loading of the LMTB (Chen et al., 1994; Li et al., 2003);

70   2) the early Jurassic rocks unconformable overly extensively folded late Triassic rocks

71   (BGMRSP, 1991; Xu et al., 1992; Burchfiel et al., 1995); 3) the pervasive orogen-

72   parallel klippen and nappe belt sitting on the foot hills of the Longmen Mountains are

73   believed related to the regional top-to-the-SE thrusting (Figure 2); 4) the consistent top-

74   to-the-SE thrusting indicated by different indicators at various scales (Xu et al., 1992;

75   Burchfiel et al., 1995; Chen et al., 1995; Chen and Wilson, 1996; Jia et al., 2006; Yan

76   et al., 2011; Yan et al., 2018); 5) the pervasive upright folding in the adjacent Songpan–

77   Ganzi Terrane was thought synchronous to the early Mesozoic deformation of the

78   LMTB (Burchfiel et al., 1995; Chen et al., 1995; Harrowfield and Wilson, 2005). This

79   prominent deformation event was constrained to *ca.* 234–200 Ma by basin tectonics,

80   timing of the top-to-the-SE/SSE shearing and syntectonic metamorphism, which

81   indicated an early Mesozoic orogeny of the LMTB (Chen et al., 1994; Li et al., 2003;

82   Yan et al., 2011; Zheng et al., 2014; Xue et al., 2016; Zheng et al., 2016; Airaghi et al.,

83   2018a; Airaghi et al., 2018b; Yan et al., 2018).

84   The early Mesozoic tectonic evolutionary mechanism accounting for the above

85   observations, however, is still in dispute. Sengör (1984) and Luo (1991) suggested that

86   the LMTB is an early Mesozoic intracontinental subduction zone accommodating

87   multi-stage crustal shortening. Then, Xu et al. (1992) proposed a bivergent subduction

88   model in which the Songpan–Ganzi Terrane sedimentary cover has been "pushed" to

89   the southeast on top of the Yangtze Block due to the bivergent subduction along the

90   Anymaqen and Jinshajiang Suture Zones. The current models suggested that the

91   Songpan–Ganzi sedimentary cover were overthrust southwards on the Yangtze Block

92   along a decollement in response to the closure of the Paleotethys (Mattauer et al., 1992;

93   Calassou, 1994; Dirks et al., 1994; Chen and Wilson, 1996; Worley and Wilson, 1996;

94   Roger et al., 2004; Harrowfield and Wilson, 2005; de Sigoyer et al., 2014; Yan et al.,

95   2018).

96   Apart from the early Mesozoic top-to-the-SE/SSE thrusting along the LMTB, an

97   increasing number of studies proposed a top-to-the-NW normal faulting that developed

98   along the NW boundary of the orogen-parallel and stripped Neoproterozoic complexes

99   (Figure 1b)(Xu et al., 2008; Zhou et al., 2008; Tian et al., 2016; Billerot et al., 2017;

100 Xue et al., 2017; Airaghi et al., 2018b). However, timing and significance of the top-

101 to-the-NW normal faulting are in dispute that have resulted in several different models,

102 such as: 1) mid-Jurassic to early Paleogene (173–160 Ma and 81–47 Ma) post orogenic

103 extension (comparing to the early Mesozoic orogeny)(Zhou et al., 2008), 2) early

104 Cretaceous (~120 Ma) crustal-scale wedge extrusion (Xu et al., 2008), 3) episodic

105 eastward basement-slice-imbrication during the late Jurassic–early Cretaceous and late

106 Cretaceous–Earliest Paleogene (Billerot et al., 2017; Xue et al., 2017), and, 4)

107 formation of a late Cretaceous–earliest Paleogene crustal scale duplex (Tian et al.,

108 2016). Based on the above compilation, most previous works have proposed that the

109 top-to-the-NW normal faulting occurred in the late Mesozoic.

110   Major questions therefore remain unsolved: 1) Considering previous early Mesozoic

111 tectonic models of the LMTB, whether did the significant shortening recorded in the

112 LMTB correspond to the imbricated thrust system during the Paleotethys' closure, or

113 to the intracontinental underthrusting along the Longmenshan belt? 2) What is the

114 tectonic significance of the top-to-the-NW normal faulting (mostly late Mesozoic) and

115 emplacement of the Neoproterozoic complexes? Therefore, an overall accurate

116 reconstruction of the Mesozoic tectonics of the LMTB and its adjacent areas, especially

117 its detailed structural analysis and timing, are of great importance.

118   This study presents detailed field investigations focusing on structural geometry and

119 kinematic reconstruction, and geochronological constraints including zircon U–Pb

120 dating of synkinematic plutonic rocks and $^{40}Ar/^{39}Ar$ dating on the synmetamorphic

121 micas of the LMTB. In conjunction with previous published geochronological and

122 metamorphic data, a new geodynamic model was proposed to interpret the Mesozoic

123 tectonic evolutionary history of the LMTB.

124

2. Geological Setting

126   At the eastern margin of the Tibetan Plateau, the LMTB separates the intensely

127 folded and metamorphosed (Greenschist facies grade) Songpan–Ganzi Terrane to the

128 NW, and the weakly/undeformed Sichuan Basin to the SE (Figure 1a). The triangle-

129 shaped Songpan–Ganzi Terrane is separated from the western Qinling–Dabie Orogenic

130 Belt to the north by the East Kunlun–Anymaqen Suture Zone, from the Qiangtang

131 Block to the southwest by the Jinshajiang Suture Zone (Figure 1a).

132   2.1 Songpan–Ganzi Terrane

133   The Songpan–Ganzi Terrane mainly comprises ~5–15 km-thick intensely folded late

134 Triassic turbidites (Calassou, 1994; Harrowfield and Wilson, 2005; Zhang et al., 2006c;

135 Zhang et al., 2008; Yin, 2015). The provenance of the turbidites includes the Kunlun

136 Mountains, North China Block, South China Block and southwest Qinling Orogenic

137 Belt (Yin and Nie, 1993; Enkelmann et al., 2007; Weislogel et al., 2010). Voluminous

138 felsic plutons intruded the Songpan–Ganzi Terrane at *ca.* 226–205 Ma, dominantly

139 derived from partial melting of the Neoproterozoic basement and sedimentary cover of

140 the Songpan–Ganzi Terrane, with negligible amounts of mantle material (Figure

141 1b)(Roger et al., 2004; Hu et al., 2005; Zhang et al., 2006b; Zhang et al., 2007; de

142 Sigoyer et al., 2014). Both geophysical and geological data indicate a continental crust

143 of Yangtze Block affinity underlying the eastern Songpan–Ganzi Terrane (Roger et al.,

144 2004; Hu et al., 2005; Zhang et al., 2009; Weislogel et al., 2010; Zhang et al., 2010;

145 Guo et al., 2013).

146   2.2 Sichuan Basin of the Yangtze Block

147   The Sichuan Basin, located in the Yangtze Block of northwest South China Block

148 (Figure 1a), preserves a Paleoproterozoic to Neoproterozoic basement overlain by

149 Neoproterozoic to Cenozoic sedimentary sequences. Silurian–Devonian abyssal

150 deposits and radiolarian chert suggested a long period of rifting during the Silurian to

151 Devonian ages along the western part of the Yangtze Block (Long, 1991; Luo, 1991;

152 Chang, 2000; Li, 2009). This rift was revealed by high-resolution seismic reflection

153 profile as well (Jia et al., 2006). During middle–late Triassic ages, coeval with the

154 southeastward thrusting and loading of the LMTB, the western Sichuan Basin began

155 subsiding flexurally and evolved into an epicontinental foreland basin (Figure 2).

156 Thrust sheets were transported to the southeast synchronously and intensely folded at

157 the end of the late Triassic (Chen et al., 1994; Chen and Wilson, 1996; Li et al., 2013c).

158 The continuous sedimentation of the middle Jurassic–upper Cretaceous deposits

159 implies a pronounced subsidence at the western Sichuan foreland basin during this

160 period (Burchfiel et al., 1995; Chen et al., 1995). Episodic SE-ward thrusting and

161 loading of the LMTB were indicated by the wedge-shaped megasequences of the

162 western Sichuan foreland basin, namely, in late Triassic–early Jurassic, late Jurassic–

163 early Cretaceous and late Cretaceous–earliest Paleocene (Xu et al., 2008; Li et al.,

164 2013c; Tian et al., 2016).

165 2.3 The LMTB

166 The NE-striking LMTB merges into the western Qinling Orogenic Belt to the

167 northeast and is truncated by the Xianshuihe Fault to the southwest (Figure 1a).

168 2.3.1 Major faults of the LMTB

169 The regional tectonic architecture of the LMTB is defined by four major NE–SW

170 striking faults, namely from the southeast to the northwest, the Anxian–Guanxian Fault

171 (T_1 in Figure 1b), the Yingxiu–Beichuan Fault (T_2 in Figure 1b), the Wenchuan–

172 Maoxian Fault (T_3 in Figure 1b), and the Qingchuan–Pingwu Fault (T_4 in Figure 1b).

173 The Anxian–Guanxian Fault dips to the northwest by 30–50° and crosscuts the late

174 Triassic–early Jurassic rocks. Approaching northwestwards, the Yingxiu–Beichuan

175 Fault dipping 40–60° to the NW separates the Sichuan foreland basin to the southeast

176 from the LMTB hinterland (BGMRSP, 1991; Xu et al., 1992; Burchfiel et al., 1995).

177 The Wenchuan–Maoxian Fault dipping 30–50° to the NW was episodically activated

178 since *ca.* 220 Ma (Burchfiel et al., 1995; Yan et al., 2008; Zheng et al., 2016). Seismic

179 reflection profile showed that the ENE-striking Qingchuan–Pingwu Fault dips to the

180 NNW or SSE at variable angles (Wang et al., 2000; Jia et al., 2006; Lin et al., 2014).

181 The northern LMTB was dissected by the Qingchuan–Pingwu Fault and incorporated

182 to northwestward- and southeastward-thrusting that resemble a positive flower

183 structure (Jia et al., 2006). The Wenchuan–Maoxian Fault and Qingchuan–Pingwu

184 Fault are characterized by mylonite overprinted by breccia and gouge (Chen and Wilson,

185 1996; Li et al., 2013a; Li et al., 2015).

186 2.3.2 Basement complexes in the LMTB

187 The basement complexes that distributes from the NE to the SW in the LMTB are

188 composed of Neoproterozoic meta-granites overlain by a Neoproterozoic meta-

189 sedimentary cover, such as the Danba (DB), Kanding (KD), Wulong (WL), Baoxing

190 (BX), Pengguan (PG), Moutuo (MT), Xuelongbao (XLB) and Jiaoziding (JZD)

191 complexes (Figure 1b). These basement complexes share similar lithology with the

192 Yangtze Block basement (BGMRSP, 1991). Field observations, Anisotropy of

193 Magnetic Susceptibility (AMS) and gravity modeling have suggested that these

194 basement complexes were strongly deformed and imbricated southeastwards as

195 basement-slices (Ma et al., 1996; Xu et al., 2008; Tian et al., 2016; Airaghi et al., 2017b;
196 Billerot et al., 2017; Xue et al., 2017).

197   2.3.3 Metamorphism in the LMTB

198   Two amphibolite facies metamorphic zones have been recognized in the meta-
199 sedimentary cover in the Wenchuan–Xuelongbao area and the Danba area (Dirks et al.,
200 1994; Huang et al., 2003a; Zhou et al., 2008; Airaghi et al., 2018a; Airaghi et al., 2018b).
201 Petrological studies (garnet–amphibolite–biotite thermometer, pseudosection using
202 Perplex modeling and chlorite–white mica–quartz thermal dynamic equilibrium)
203 constrain the peak metamorphic conditions at ~11 ± 2 kbar, ~620 ºC in the Wenchuan–
204 Xuelongbao area (Dirks et al., 1994; Airaghi et al., 2018a) and ~5.3–8 kbar, 570–680
205 ºC in the Danba area (Huang et al., 2003a; Weller et al., 2013). The Wenchuan–
206 Xuelongbao metamorphic belt reached amphibolite facies conditions at *ca.* 210–180
207 Ma (Airaghi et al., 2018a; Airaghi et al., 2018c) and recorded fast exhumation at *ca.*
208 140–120 Ma (Arne et al., 1997; Airaghi et al., 2018c). The Danba amphibolite-facies
209 metamorphic belt reached peak conditions at *ca.* 205–180 Ma (Huang et al., 2003a;
210 Weller et al., 2013) and initiated enhanced rapid cooling at *ca.* 168–158 Ma (Huang et
211 al., 2003a; Zhou et al., 2008).

212   Apart from these two amphibolite facies metamorphic zones, late Triassic
213 blueschists occur as lenses along the Qingchuan–Pingwu Fault, with peak metamorphic
214 pressure attained to 5.2–6.5 kbar (Wei, 1994; Xu et al., 2020). The blueschist then have
215 been retrograded to greenschist in a nearly isothermal decompression way (Wei, 1994).

216   2.3.4 Tectonic events of the LMTB

217   The LMTB recorded at least three phases of deformation, including (1) D_1, the late
218 Triassic to early Jurassic regional top-to-the-SE thrusting, (2) D_2, the top-to-the-NW/N
219 normal faulting of poorly constrained timing and tectonic significance, and (3) D_3, the
220 Cenozoic shortening reactivation (Xu et al., 1992; Burchfiel et al., 2008; Richardson et
221 al., 2008; Xu et al., 2008; Li et al., 2013a; Li et al., 2015; Tian et al., 2016; Xue et al.,
222 2017). The D_1 deformation is well identified by penetrative cleavages (S_1), mineral and
223 stretching lineation (L_1) in the Wenchuan area, and the top-to-the-SE thrust sheets and
224 nappes over the intensely folded late Triassic sequences in the western Sichuan foreland
225 basin (Xu et al., 1992; Burchfiel et al., 1995; Worley and Wilson, 1996; Li et al., 2003).
226 Most parts of the Songpan–Ganzi Terrane show slow cooling rate at *ca.* 1°C/Ma since
227 the early Mesozoic (Huang et al., 2003a; Huang et al., 2003b; Roger et al., 2011).

228 However, an enhanced cooling event (*ca.* 8°C/Ma) during the late Jurassic to Eocene

229 was reported at the peripheries of the Songpan–Ganzi Terrane, especially in the

230 Wenchuan and Danba areas (Yuan et al., 1991; Arne et al., 1997; Huang et al., 2003a).

231 This rapid cooling event probably responded to the D_2 top-to-the-NW/N normal

232 faulting. The belt characterized by the top-to-the-NW normal faulting developed along

233 the northwest/north boundary of the basement complexes was entitled as the East Tibet

234 Detachment (Wang et al., 2012b). The D_3 deformation was thought to have initiated

235 since *ca.* 30–25 Ma that builds the present Longmen mountains of the eastern Tibetan

236 Plateau (Clark and Royden, 2000; Kirby et al., 2002; Wang et al., 2012a).

237

238 **3. Structural analysis of the LMTB**

239   3.1 Structural subdivisions of the LMTB

240   The LMTB was interpreted as an allochthonous sheet thrusting southeastward upon

241 the autochthonous western Sichuan Foreland Basin (Xu et al., 1992; Burchfiel et al.,

242 1995; Worley and Wilson, 1996; Robert et al., 2010a). Based on structural

243 investigations, we present revised structural subdivisions of the LMTB. Firstly, the

244 LMTB is divided into a Southeastern Zone and a Northwestern Zone by a Main Central

245 Boundary (see Section 3.2; Figure 3a). According to the lithology, deformation

246 intensity, and metamorphic grade, the Southeastern Zone can be further subdivided into

247 four subdivisions (Figure 3). They are, from the southeast to the northwest: i) the

248 undeformed Autochthon that comprises the western part of the Sichuan Foreland Basin,

249 ii) the Para-autochthon, transported southeastwards along the Anxian–Guanxian Fault

250 and rests over the Autochthon, iii) the Allochthon that traveled southeastwards much

251 further on top of the Para-autochthon, and iv) the Inner Metamorphic Core that recorded

252 the highest metamorphic conditions (*i.e.*, amphibolite facies) among the Southeastern

253 Zone. The four subdivisions in the Southeastern Zone are separated by the three major

254 listric faults of the LMTB (Figure 3; see in Section 2.3.1).

255   i) The Autochthon, located to the southeast of the Anxian–Guanxian Fault, is mainly

256 composed of Jurassic–Cretaceous strata and overlying Cenozoic sediments (Figures 3

257 and 4). The Jurassic–Cretaceous strata were deposited in circumstances of alluvial,

258 fluvio-deltaic, and lacustrine fills, characterized by medium and coarse-grained

259 sandstone with some conglomeratic layers at the base. Total thickness of the Jurassic–

260 Cretaceous sequences is more than 5 km (BGMRSP, 1991). In the northern part of the

261 LMTB, close to Anxian and Jiangyou county, the early Jurassic and overlying
262 Cretaceous to Cenozoic sequences are dipping to the southeast that unconformably rest
263 on the intensively folded late Triassic rocks (Figures 2 and 4c–d)(BGMRSP, 1991).

264   ii) The Para-autochthon is sandwiched by the Anxian–Guanxian Fault and the
265 Yingxiu–Beichuan Fault, with its half area covered by klippen and nappes from the
266 Allochthon (Figure 3). The Late Triassic Xujiahe Formation dominated in this
267 subdivision either passes up from the earliest late Triassic marine sandstone or
268 unconformably overlies the middle Triassic limestone (Li et al., 2003; Meng et al.,
269 2005). The Xujiahe Formation shows markable lateral variation in both thickness and
270 sedimentary facies. Coarse-grained sediments, such as alluvial conglomerate bodies
271 occur close to the Yingxiu–Beichuan Fault, but change into fine-grained lacustrine
272 sediments toward to the basin interior.

273   iii) The Allochthon is mainly exposed between the Wenchuan–Maoxian Fault and
274 the Yingxiu–Beichuan Fault, and also includes the klippen and nappes resting on top
275 of the Para-autochthon (Figures 2 and 3a). Northwest to the Yingxiu–Beichuan Fault,
276 this subdivision mainly consists of Silurian shale and greywacke with the bedding
277 completely transposed into foliation. Greenschist-facies metamorphism is indicated by
278 mineral assemblages of fine-grained muscovite + chlorite + quartz (Airaghi et al.,
279 2017b; Xue et al., 2017). Metamorphic condition jumps of ~50 ºC, 3–5 kbar
280 southeastwards across the Yingxiu–Beichuan Fault suggest that the Allochthon are
281 more deformed and metamorphosed in a deeper structural level than the Para-
282 autochthon (Robert et al., 2010a; Airaghi et al., 2018b). Neoproterozoic complexes
283 including the Pengguan and Jiaoziding complexes are distributed in this subdivision.
284 Southeast to the Yingxiu–Beichuan Fault, klippen and nappes are mainly composed of
285 Devonian to early Triassic thick-bedded limestone and marine sandstone (Figures 2, 3
286 and 4a–d).

287   iv) The Inner Metamorphic Core comprises phyllite and micaschist that are mostly
288 metamorphosed Silurian sediments (Figures 2 and 3). Amphibolite-facies metamorphic
289 zone that wraps the oval-shaped Xuelongbao (XLB in Figure 2) and stripped Moutuo
290 (MT in Figure 2) complexes records the highest-grade metamorphism within the
291 Southeastern Zone (Dirks et al., 1994; Airaghi et al., 2017a; Airaghi et al., 2018a). Peak
292 P–T condition attained to ~11 ± 2 kbar and ~620 ºC at the southernmost margin of the
293 Xuelongbao complex calculated from metamorphic assemblages of biotite + garnet +

294   staurolite + muscovite + kyanite (Dirks et al., 1994; Airaghi et al., 2018a). Based on

295   the enhanced metamorphic grade and deformation intensity, the Inner Metamorphic

296   Core are therefore more deformed and metamorphosed in a deeper structural level than

297   the Allochthon.

298   The Northwestern Zone includes eastern Songpan–Ganzi Terrane with

299   Neoproterozoic sequences outcropped in the north and Paleozoic sequences outcropped

300   in the south (Figures 2 and 3). The northern Northwestern Zone mainly consists of two

301   Neoproterozoic Groups, namely, 1) the volcanic Bikou Group defined by mafic lavas

302   within its lower part and ranges from mafic to intermediate–felsic within its upper

303   portion, and 2) the Hengdan Group tectonically resting on the Bikou Group is composed

304   of black, thin-bedded pyrite-bearing shales and interbedded thinly volcaniclastic

305   sandstone and siltstone (Yan et al., 2003; Druschke and Wang, 2006). The southern

306   Northwestern Zone includes Devonian Weixian Formation and the Triassic sequences.

307   The Devonian sequences consist mainly of quartziferous phyllite to schist and

308   interbeded quartzite. The overlying Triassic Xikang Group is dominated by thick and

309   highly repetitious flysch sediments. Although different rock units comprising the

310   northern and southern Northwestern Zone, it was metamorphosed under similar

311   greenschist facies conditions (Figures 1b and 2)(Xu et al., 1992; Liu et al., 2008)

312

313   3.2 The Main Central Boundary

314   The Main Central Boundary serves as a major tectonic boundary separating the

315   Northwestern Zone and the Southeastern Zone. It corresponds to the southern branch

316   of the Qingchuan Fault (T$_4$ in figure 2) in the north (BGMRSP, 1991), and to a vertical

317   cleavage zone within the Paleozoic rocks in the south (Figure 2). To the SE of the Main

318   Central Boundary, all structural planes in the Southeastern Zone, including foliations,

319   cleavages, and fold axial planes, are exclusively dipping to the NW. Various kinematic

320   indicators in the Southeastern Zone suggest a consistent top-to-the-SE/S thrusting. To

321   the NW of the Main Central Boundary, the Northwestern Zone is characterized by the

322   SSE-dipping planar structures and associated top-to-the-NW thrusting (Figure 3).

323   The Qingchuan–Pingwu Fault, as the northern segment of the Main Central

324   Boundary, is a major tectonic boundary. Seismic profiles, drill data (Jia et al., 2006)

325   and field observations indicate that the Qingchuan–Pingwu Fault is a positive flower

326   structure developed in a transpressional system. Microfabric study (Wang et al., 2000)

327   indicated that the Qingchuan–Pingwu Fault was originated from a deep-seated ductile

328   shear zone during late Triassic and overprinted by Cenozoic brittle deformation at very

329   least. It is the late Triassic deep-seated ductilely sheared Qingchuan–Pingwu Fault

330   rather than the Cenozoic brittle one that separates the LMTB into the Southeastern Zone

331   and Northwestern Zone.

332   The southern segment of the Main Central Boundary roughly distributes along the

333   geological boundary between the Silurian and Devonian–Permian sequences (Figure 2).

334   Macroscopically, this segment of Main Central Boundary shows predominant vertical

335   cleavage and foliation within intensely deformed argillaceous limestone, graphitic

336   pelite and thin-bedded limestone–quartz ribbon interlayers (Figures 3a and 5). Their

337   bedding (S_0) can be distinguished by the compositional variations that is parallel to the

338   cleavages (Figure 3a and 5b). Associated rootless folds imply significant shortening

339   during the formation of the Main Central Boundary (Figures 3a and 5b–c). P-wave

340   receive function and seismic reflection profiles revealed a Moho at ∼36–40 km depth

341   beneath the Sichuan Basin that gradually deepens northwestwards at ∼63 km depth

342   beneath the eastern Tibet (Guo et al., 2013). This transition occurs beneath the

343   Wenchuan Shear Zone (corresponding to Inner Metamorphic Core) over a horizontal

344   distance of fewer than 30 km (Robert et al., 2010b; Zhang et al., 2010; Guo et al., 2013).

345   Geophysical profiles, therefore, support the statement that the southern Main Central

346   Boundary, as the northwest boundary of the Inner Metamorphic Core, serves as a major

347   tectonic boundary.

348   3.3 The main deformation (D_1)

349   The D_1 main deformation is defined by a NW–SE striking stretching lineation

350   recognized in both the Southeastern and Northwestern zones which is separated by the

351   Main Central Boundary (Figure 2). Kinematic indicators indicate a top-to-the-SE

352   thrusting and a top-to-the-N/NW thrusting in the Southeastern and the Northwestern

353   zones, respectively. Since there is no evidence of superposition between these two

354   senses of shear, it is difficult to precisely define the relative timing of these opposite

355   shearing events. Nevertheless, to clarify the presentation of the deformation events, in

356   the following, we distinguish D_{1E}, the top-to-the-SE thrusting in the Southeastern Zone,

357   and D_{1W}, the top-to-the-NW/N thrusting in the Northwestern Zone, respectively.

358   3.3.1 Top-to-the-SE thrusting in the Southeastern Zone (D_{1E})

359   The top-to-the-SE shearing and thrusting are widespread in the Southeastern Zone
360   at variable scales, except that the Autochthon merely recorded long-wavelength fold
361   and monoclines toward the interior of the Sichuan Basin (Figure 4). The D_{1E} top-to-
362   the-SE thrusting is most developed in the Inner Metamorphic Core and generally
363   attenuated southeastwards.

364   The Inner Metamorphic Core was ductilely deformed showing predominant NW-
365   dipping foliation (S_1) at varied angles between 60–90°. Specifically, the foliation
366   gradually steepens when approaching the Main Central Boundary, and eventually
367   presents in a vertical attitude (Figures 2–4). This changing trend of foliation implies
368   that the deformation intensified toward the Main Central Boundary. Foliations mostly
369   consist of an alternation of biotite-white mica-rich and light-colored, pelitic interlayers
370   (Figures 3a and 6a–b). Along the transect from Wenchuan county to Xuecheng town,
371   an NW-plunging mineral and stretching lineation (L_1) defined by aligned newly formed
372   biotite, white mica, elongated quartz aggregates, or iron-oxide pods are well developed
373   (Figures 3a and 6a). Kinematic indicators document a consistent top-to-the-SE
374   thrusting in the Inner Metamorphic Core. Such as asymmetric pyrite pressure shadow
375   in mica-schist (Figures 3a and 6b) and sigma-shaped feldspar porphyroclasts in
376   paragneiss (Figures 3a and 6c) both show top-to-the-SE thrusting. Photomicrographs
377   (perpendicular to the foliation and parallel to the lineation) show that newly formed
378   white mica oriented as compaction plane (S) and shear plane (C), both of which
379   composes an S-C fabric documenting a consistent top-to-the-SE thrusting (Figures 3a
380   and 6d).

381   In the Allochthon, the Neoproterozoic complexes such as the Pengguan and
382   Jiaoziding complexes, mostly show brittle deformation characterized by subhorizontal
383   joints. Inside the Pengguan complex, several NE–SW trending ductile shear zones
384   dissected and thrust the granitic rocks to the southeast (Airaghi et al., 2017b; Xue et al.,
385   2017). Upon the granitic rocks, the Neoproterozoic Huangshuihe Group recorded
386   extensive shearing and sigmoid pelitic lens incorporated to the top-to-the-SE thrusting
387   (Figures 3a and 6e). Structural planes including axial planar cleavages and spaced
388   cleavages dip to the northwest at angles of 30–65° (Figures 2–4). Fine-grained white
389   mica and chlorite are developed on these structural planes demonstrating a greenschist
390   facies grade of deformation. Sigma-shaped sandy lens in the Silurian pelitic schist
391   indicate a top-to-the-SE thrusting as well (Figures 3a and 6f).

392   As part of the Allochthon, most of the klippen are synclines overturned to the SE,

393   with SE-ward reverse fault which dissected the thick Devonian limestone at the rear of

394   the klippe (Figures 2 and 6g), and show a consistent top-to-the-SE thrusting (BGMRSP,

395   1991).

396   In the Para-autochthon, the late Triassic Xujiahe sandstone is intensively folded as

397   indicated by the NE-SW trending π-circle-projected axis of bedding (Figures 3b-d). In

398   the south part, multi π circle-Axis exist roughly trending NE-SW, implying multiphase

399   of shearing and thrusting. Folds are mostly overturned to the SE indicating a top-to-

400   the-SE thrusting (Figure 2). Axial planar cleavages are locally developed that gradually

401   intensified and more penetrative approaching northwestward to the Yingxiu–Beichuan

402   Fault. This cleavage-enhancing trend implies a northwestward increase in deformation

403   intensity. In mudstone–sandstone interlayered rocks, competence contrast facilitates

404   the formation of layer-parallel slip and shearing. Sigmoid lens as well as "cold" shear-

405   band fabrics consistently indicate a top-to-the-SE thrusting (Figures 3a and 6h).

406   In the Autochthon, lower Jurassic strata and overlying continuous Cretaceous–

407   Cenozoic sequences are mostly concordantly folded in a long-wavelength way. The

408   fact that early Jurassic rocks locally overturned to the southeast (North to the Tangbazi

409   town; Figure 2) therefore implies a post-Jurassic reactivation of the SE-directed

410   thrusting (Figures 2 and 4d).

411   3.3.2 Top-to-the-NW/N thrusting in the Northwestern Zone (D_{1W})

412   The structures and kinematics within the Northwestern Zone are different from those

413   within the Southeastern Zone. In the northern Northwestern Zone, S-dipping foliation

414   and associated downdip lineation are well developed. Lineations are defined by aligned

415   calcite, fine-grained white mica, and oxide pods (Figures 2, 3a and 7a). Along the

416   lineation, a consistent top-to-the-N/NW shearing and thrusting is determined by various

417   kinematic indicators, such as sigma-shaped pebbles in strongly sheared meta-

418   conglomerate (Figures 3a and 7b) and asymmetric pressure shadow in sandy–pelitic

419   schist. Photomicrographs show that quartz ribbon (Figures 3a and 7c) and sigma-shaped

420   feldspar porphyroclasts (Figures 3a and 7d) both indicate a top-to-the-N thrusting. In

421   the north of the Pingwu city, greywacke and siltstone were extensively folded verging

422   to the north with associated meter-scale reverse fault cutting fold limbs (Figures 3a and

423   7e). West to the Pingwu city, bedding (depicted by compositional banding) completely

transposed to SE-dipping foliations in response to the northward shearing and thrusting (Figures 3a and 7f).

In the southern Northwestern Zone, axial planar cleavage developed in the thin-bedded limestone mostly dips to the SE but strikes roughly along the margin of the Xuelongbao complex (Figure 2). On the foliation, lineation plunges to the SE at ~65–70° (Figures 2 and 3a). Along the lineation, asymmetric pressure shadow of calcite tail around garnet pseudomorph indicates a top-to-the-NW thrusting (Figures 3a and 7g). Asymmetric NW-verging folds are developed at different scales. The late Triassic turbidite was involved in a hundred-meter scale chevron fold verging to the NW that is consistent with the top-to-the-NW thrusting (Figures 3a and 7h). In the whole Northwestern Zone, the top-to-the-NW/N thrusting is indicated by the pervasive NW/N-overturned bedding as well (Figure 2)(BGMRSP, 1991).

3.3.3 Syntectonic (D_{1W}) Mupi pluton in the Northwestern Zone

In the Northwestern Zone, north of the Pingwu city, the Mupi pluton is a coarse-grained diorite and granodiorite pluton with prominent syntectonic features (Figure 2). At its southern margin, the contact between the pluton and the country rock is rather ambiguous. Strong mylonitisation with S-dipping foliation deformed both the country rocks and the south margin of the pluton (Figures 3a and 8c). On the S-dipping foliation (S_1), aligned biotite and sheared feldspar define a mylonitic lineation plunging south at ~45–75°. Kinematic indicators including sigmoidal feldspar porphyroclasts and shear-bands both indicate a top-to-the-N shearing related to thrusting (Figures 3a and 8d). About 10–15 meters northwards from the south margin of the pluton, a set of quartz + feldspar veins parallel to the shear foliation (Figures 3a and 8b), in which the quartz and feldspar did not record ductile deformation. Further north ~30 meters from the south margin of the pluton, the pluton rocks show magmatic fabric with euhedral feldspar randomly distributed (Figures 3a and 8a). Cracks in feldspar grains are sub-parallel to the shear planes and infilled with quartz (Figures 8e and S1). These cracks in conjunction with the foliation-parallel quartz + feldspar veins indicate that a brittle deformation of the feldspar occurred in the presence of residual melt. Therefore, based on the textural criteria proposed by Paterson et al. (1989), we prefer to interpret the Mupi pluton as a syntectonic one relating to the D_{1W} deformation.

456   3.4 Top-to-the-NW normal faulting along the northwest boundary of the basement

457   complexes (D_2)

458   Most of the Neoproterozoic basement complexes in the Southeastern Zone are

459   devoid of ductile deformation but characterized by widespread subhorizontal joints

460   (Xue et al., 2017). Mylonite is localized along the northwest boundary of the

461   Xuelongbao and Pengguan complexes. Along the western boundary of the Xuelongbao

462   complex, foliation dips to the NW at 45–80° with lineation plunging to the west (Figure

463   2). These structural foliations and lineations are difficult to distinguish from those of

464   the D_{1E} deformation structures. However, sigmoidal feldspar clasts and S/C fabric

465   indicate different kinematics of top-to-the-NW normal faulting (Figures 3a and 9a). The

466   Silurian rock directly overlies the Neoproterozoic Pengguan complex also supports

467   NW-ward normal faulting (Figure 2).

468   Along the northwest boundary of the Pengguan complex, mylonitic foliation dips to

469   the NW at high angles of ~80° (Figures 3a and 9b) with lineation steeply plunging to

470   the NW, except for a few SE- or N-dipping foliations that probably resulted from tilting

471   of the original foliations by the Cenozoic deformation (Figure 2). Photomicrographs

472   including asymmetric mica fishes (Figures 3a and 9c), sigmoidal feldspar

473   porphyroclasts (Figures 3a and 9d), and S/C fabric of white mica (Figures S2c and e)

474   indicate a top-to-the-NW normal faulting. The deformed rocks experienced syntectonic

475   greenschist-facies metamorphism with a mineral assemblage of quartz + feldspar +

476   biotite + white mica + chlorite (Figures S2e–f).

477   Microscopic structures from the northwest Pengguan complex show sigma-shaped

478   porphyroclast, quartz ribbon (Figures 3a and 9f), and white mica shear-band fabric

479   (Figures 3a and 9g), indicating a top-to-the-SE shearing related to the D_{1E} deformation.

480   However, all these structures are cut by NW-dipping shear-bands (Figures 3a and 9e).

481   In the western flank of the Wulong complex, about 60 km southwest to the Pengguan

482   complex, a similar top-to-the-NW normal fault with greenschist-facies metamorphism

483   that cuts D_{1E}-related thrust sheet has been previously reported as well (Figure

484   1b)(Burchfiel et al., 1995; Tian et al., 2016; Airaghi et al., 2018b). Thus, we interpret

485   the top-to-the-NW normal faulting in the northwest Pengguan complex and the

486   Xuelongbao complex as the D_2 event after the D_{1E} top-to-the-SE thrusting in the

487   Southeastern Zone.

488

4. Geochronological constraints

In order to constrain the timing of the D_1 double-vergent thrusting and the D_2 top-to-the-NW normal faulting, SIMS U–Pb dating on zircons from the synkinematic Mupi pluton and ^{40}Ar-^{39}Ar dating on metamorphic white mica, biotite and fine-grained white mica were carried out.

4.1 Analytical methods

4.1.1 Zircon SIMS U-Pb dating

Zircon concentrates were extracted using conventional crushing and separation techniques. After set in epoxy resin mounts, mineral grains were polished to their cores. Cathodoluminescence (CL) imaging was performed to observe their internal structure and find suitable positions for spot analyses. Geochronological data were acquired at the State Key Laboratory of Lithospheric Evolution, Institute of Geology and Geophysics, Chinese Academy of Sciences (IGGCAS).

U–Pb zircon dating was conducted on a Cameca IMS–1280HR SIMS following the analytical procedures described by Li et al. (2009). The primary O^{2-} ion beam was focused to elliptical spots with the sizes of 20 μm×30 μm. Measured Pb/U ratios were calibrated relative to the zircon standard Plešovice (Sláma et al., 2008). Non-radiogenic Pb was subtracted from the measured Pb isotopic composition using the measured ^{204}Pb and the present-day average terrestrial Pb isotopic composition in the model of (Stacey and Kramers, 1975). U–Pb data were plotted and calculated using the program Isoplot 3.00 (Ludwig, 2003), and age uncertainties are quoted at the 95% confidence level except for those noted otherwise. Measurements on a second zircon standard Qinghu were interspersed with unknowns to monitor the external uncertainties, and yielded concordia ages of 159.6 ± 1.6 Ma (MSWD = 0.28, N = 6), which are identical within errors to the recommended age (159.5 ± 0.2 Ma)(Li et al., 2013b).

4.1.2 ^{40}Ar-^{39}Ar dating

Micas were separated from eight micaschist, gneiss, and mylonite samples for ^{40}Ar/^{39}Ar dating by step-heating technique. Minerals were irradiated and measured in the Ar-Ar Laboratory, School of Earth Sciences of the University of Melbourne. Hand-picked grains were cleaned in de-ionized water and acetone. Samples were weighted and loaded into aluminum packets for irradiation. The packets were placed in a silicate glass tube (Can UM#80), interleaved with packets containing the flux monitor Mount Dromedary Biotite (Age = 99.125 ± 0.076 Ma)(Phillips et al., 2017). The canister was

irradiated for 40 MWhr in the CLICIT facility of the Oregon State University TRIGA reactor, USA. The measured isotopic ratios were corrected for system blanks, mass discrimination, and irradiation-induced interference. Plateau and/or total gas ages with 2σ uncertainties were calculated and calibrated based on methods proposed by (Lee et al., 2006). Analytical data are presented in Table S2 (Xue et al., 2020), and the age spectra are presented in Figure 11. Argon age plateaus are defined by contiguous gas fractions that together represent more than 50% of the total ^{39}Ar released from the sample and for which no difference in age can be detected between any two fractions at the 95% confidence level (Fleck et al., 1997). According to this definition, all argon age spectra in this work, except for sample CX33, do not yield plateau ages (Figure 11). We choose contiguous steps within 95% confidence close to 50% of the total ^{39}Ar released (CX6A white mica), or contiguous steps close to 95% confidence more than 50% of the total ^{39}Ar released (CX2, CX6B, CX25, CX44 white mica), to calculate weighted mean ages (Figure 11).

4.2 Results

4.2.1 U–Pb dating on synkinematic Mupi pluton

Zircons from the Mupi pluton are pink to colorless, 80 to 200 μm long with length/width ratios from 2 to 3. They show well-developed crystal morphologies. CL images of zircons show that most of the zircons have well-developed oscillatory zoning of igneous origin and some grains have an inherited core (Figure 10a). Under guidance of the zircon CL images, analyzed spots were positioned on the oscillatory zircon mantle/margin when there are exist inherited zircon cores. SIMS U–Pb zircon results are listed in Table S1. The SIMS U–Pb dating of the Mupi pluton yields a concordant age of 219.1 ± 1.7 Ma (MSWD = 0.99, N = 15; Figure 10b).

4.2.2 ^{40}Ar-^{39}Ar dating

Sample CX44 collected from the northern Northwestern Zone (Figure 12) is micaschist with penetrative SSE-dipping foliation and associated S-plunging lineation related to the D_{1W} top-to-the-N thrusting. The CX44 micaschist contains domains rich in fine-grained white mica and quartz that define the shear foliation (Figures S2a–b). Multi-grain white mica (211–152 μm) separated from CX44 yields a weighted mean age of 224.1 ± 1.7 Ma, accounting for 81% of released ^{39}Ar (Figures 11a and Table 1).

554   Sample CX12 collected from the southern Northwestern Zone (Figure 12) is
555   micaschist involved in the D_{1W} top-to-the-NW thrusting. Shear foliation is defined by
556   aligned fine-grained white mica (Figure 7g). Two aliquots of fine-grained white mica
557   (104–66 μm) of CX12A & CX12B show discordant stair-shaped spectra increasing
558   from ~65–70 Ma to ~150 Ma and ~120 Ma, respectively (Figures 11b–c and Table 1).

559   Samples CX6 and CX33 (Figure 12), collected from the Inner Metamorphic Core
560   within the Southeastern Zone, are characterized by penetrative NW-dipping foliation
561   and NW-plunging lineation that was involved in D_{1E} top-to-the-SE thrusting. In these
562   two samples, the foliations and associated lineations are defined by white mica (Figures
563   6d and S2g). Two aliquots of white mica (152–211 μm) of CX6A and CX6B yield
564   equivalent weighted mean ages of 124 ± 1.9 Ma and 126.3 ± 3.3 Ma, respectively
565   (Figure 11d–e). Multi-grain white mica (152–211 μm) from CX33 yields a plateau age
566   of 148.2 ± 1.2 Ma (>60% of the total ^{39}Ar; Figure 11f and Table 1).

567   Samples CX25 from micaschist of the Xuelongbao complex and CX18, CX19 from
568   gneiss/mylonite of the Pengguan complex (Figures 12) show well-developed NW-
569   dipping foliations related to the D_2 top-to-the-NW normal faulting (Figures S2c–f).
570   White mica (211–152 μm) in CX25 that defines the shear planes (Figures S2e–f) was
571   selected for ^{40}Ar/^{39}Ar dating. Five steps of sample CX25 with ~80% released ^{39}Ar
572   yields a weighted mean age of 79.7 ± 2.7 Ma (Figure 11h). Samples of CX18 and CX19
573   have stair-shaped spectra, in which ages increase from ~50–60 Ma to ~110–135 Ma
574   from low- to high-temperature steps (Figure 11i–k and Table 1).

575   Sample CX2 from the northwest boundary of the Pengguan complex (in a structural
576   position equivalent to the samples CX18 and CX19; Figure 12) was involved in the D_2
577   top-to-the-NW normal faulting (Figures 3 and 9g–i). Multi-grain white mica (211–152
578   μm) from CX2 yields a weighted mean age of 26.23 ± 0.99 Ma at low- to medium-
579   temperature steps (>50% of the total ^{39}Ar released; Figure 11g and Table 1).

580

581   4.3 Interpretation of the geochronological results

582   4.3.1 Zircon U-Pb data interpretation

583   In the northern Northwestern Zone, the Mupi pluton shows a continuous transition
584   from mylonitic fabrics along the pluton margin to magmatic fabrics in the pluton
585   interior, arguing for its synkinematic emplacement. This deduction is supported by the
586   fact that quartz + feldspar veins parallel to the mylonitic foliation, and feldspar records

587 brittle deformation occurred in the presence of residual melt (see details in Section

588 3.3.3). Thus, the D_{1W} top-to-the-N/NW thrusting is closely related to the emplacement

589 of the Mupi pluton. Our zircon U–Pb ages reveal that the Mupi pluton emplaced at *ca.*

590 219 Ma, therefore place age constraint on the D_{1W} top-to-the-N/NW thrusting at *ca.*

591 219 Ma (Figure 12).

592   4.3.2 ^{40}Ar-^{39}Ar data interpretation

593   All samples show high radiogenic ^{39}Ar and almost all steps are clustered at the

594 horizontal ^{39}Ar/^{40}Ar axis that does not define a real inverse isochron line (Table S2;

595 Figure S3). Most of the step-ages calculated both by using initial ^{40}Ar/^{36}Ar of 298.56

596 (Lee et al., 2006) and from the so-called inverse isochron show nearly no difference

597 (Table S2). Thus, the inverse isochron ages (though identical to their weighted mean

598 ages or plateau ages) and the fake extraneous atmosphere argon are meaningless and

599 will not be further discussed (Figure S3; Table S2).

600   Concordant white mica ^{40}Ar-^{39}Ar spectra, such as those yielded by samples of CX44

601 (81.6% released ^{39}Ar), CX6A (49.5% released ^{39}Ar), CX6B (52.4% released ^{39}Ar),

602 CX33 (60.1% released ^{39}Ar), CX2 (53.6% released ^{39}Ar) and CX25 (79.7% released

603 ^{39}Ar), are typical of samples that have remained a closed system since

604 thermal/mylonitic resetting or crystallization (Figures 11a and d–h). Similar rocks to

605 sample CX44 recorded greenschist facies metamorphism under temperatures of 260–

606 310 °C (chlorite + white mica multi-equilibrium thermometer; Liu et al., 2008), which

607 is lower than the white mica argon closure temperature of *ca.* 425 °C (100 μm

608 grain)(Harrison et al., 2009). Considering that the dated mica grains are strongly

609 deformed by the top-to-the-N/NW thrusting, we, therefore, interpret that the 224.1 ±

610 1.7 Ma argon age of CX44 recorded the timing of the white mica recrystallization

611 related to the D_{1W} thrusting event.

612   Samples of CX6A & CX6B, and CX33 from the Inner Metamorphic Core, CX2 and

613 CX25 from the mylonite zone along the northwest boundary of the Pengguan and

614 Xuelongbao complexes have been deformed and metamorphosed at temperatures

615 of >530°C (Raman Spectroscopy on Carbonaceous Material; Robert et al., 2010b).

616 These temperatures are higher than the closure temperature (425 °C) of the *ca.* 100 μm

617 radius muscovite grain (Harrison et al., 2009). There is no evidence of any post late

618 Cretaceous to Cenozoic magmatism along the LMTB and its adjacent eastern Songpan–

619 Ganzi Terrane. Thus, the flattened spectra of CX6A (124 ± 1.9 Ma), CX6B (126.3 ±

620 3.3), CX33 (148.2 ± 1.2 Ma), CX2 (26.2 ± 0.9 Ma), and CX25 (79.7 ± 2.7 Ma) are

621 probably cooling ages when deformation rapidly exhumed those rocks through the ca.

622 425 °C geothermal depth. These cooling ages, therefore, can represent the timing of

623 deformations. In this scenario, considering samples of CX6A, CX6B and CX33 were

624 involved in top-to-the-SE thrusting, we interpret the dates of 148 Ma and 124 Ma as

625 ages to SE-ward thrusting and rapid exhumation. Samples of CX2 and CX25 collected

626 from the northwest boundary of the Pengguan and Xuelongbao complexes were

627 involved in top-to-the-NW normal faulting, which may imply that the top-to-the-NW

628 normal faulting occurred at *ca.* 27 Ma along the northwest boundary of the Pengguan

629 complex, and at *ca.* 80 Ma along the northwest boundary of the Xuelongbao complex,

630 respectively.

631   Discordant stair-shaped spectra, such as those observed from the samples of CX12,

632 CX18, and CX19 (Figures 11b–c, i–k), are commonly observed in fine-grained mineral

633 mixes (Tian et al., 2016). Those staircase spectra indicate ^{40}Ar diffusive loss that is

634 possibly related to chemical alteration, a subsequent thermal event disturbance, or

635 argon loss during the late stage mylonitisation (Costa and Maluski, 1988; Lovera et al.,

636 1989; West and Lux, 1993). The oldest age of the stair-shaped spectra is a minimum

637 one for the fine-grained white mica closure age (McDougall and Harrison, 1988).

638 Samples of CX12, CX18, and CX19 have been deformed at temperatures >530°C as

639 well (Raman Spectroscopy on Carbonaceous Material; Robert et al., 2010).

640 Considering the size of white mica (104–66 μm), the argon-argon system of fine-

641 grained mica should be completely reset (Harrison et al., 2009). According to the stair-

642 shaped spectra, samples of CX12A, CX12B, CX18, CX19A, CX19B may have

643 recrystallized or been reset before 146.5 ± 2.7 Ma, 119 ± 1.3 Ma, 111.1 ± 0.2 Ma, 133.7

644 ± 3.3 Ma, and 139.3 ± 1.1 Ma, respectively (Figures 11b–c, i–k). These oldest ages of

645 the stair-shaped spectra possibly resulted from the 148–124 Ma mylonitisation as

646 implied by ^{40}Ar-^{39}Ar cooling ages of CX6A, CX6B, and CX33.

647   Chemical alteration should have led to a more profound influence on the fine-

648 grained white mica of CX12, CX18, and CX19 that may result in ^{40}Ar diffusive loss

649 and flattened spectra (Harrison et al., 2009). In this way, considering samples of CX2,

650 CX18, CX19, and CX25 located at the same structural position along the northwest

651 boundary of the Neoproterozoic complexes, we may expect that CX2 and CX25,

652 showing stair-shaped spectrum and CX18, CX19 and presenting flattened spectra, yield

653   younger ages, however, it is not the case (Figures 11g–k). Thus, chemical alteration

654   and related ^{40}Ar diffusive loss may not be the main factor to account for the stair-shaped

655   spectra.

656   An alternative interpretation may suggest that the youngest age of the stair-shaped

657   spectra gives a maximum age of the thermal overprint or late-stage mylonitisation

658   (Costa and Maluski, 1988; Lovera et al., 1989; West and Lux, 1993). As stated above,

659   no magmatism of late Mesozoic–Cenozoic ages has been reported along the LMTB.

660   Thus, the post-cooling thermal event may not be responsible for the minimum ages of

661   the stair-shaped spectra. The youngest ages in the stair-shaped spectra therefore most

662   likely indicate late-stage mylonitisation after ~60–50 Ma (Figures 11i–k), which

663   possibly related to the *ca*. 27 Ma top-to-the-NW faulting along the northwest boundary

664   of the Pengguan complex. It is worth to note that the CX12A and CX12B fine-grained

665   white mica from the Northwestern Zone (Figure 12), far away from the Pengguan

666   complex, show older minimum ages of 64.7 ± 1.3 Ma and 72.2 ± 1.4 Ma comparing

667   with the 50 ± 0.1 Ma, 59 ± 0.3 Ma, and 58.4 ± 0.4 Ma of the CX18, CX19A and CX19B

668   (Figures 11b–c, j–l), which may suggest that the CX12 has been less affected by the

669   top-to-the-NW normal faulting comparing to the CX18 and CX19.

670

5 Discussion

5.1 Summary of our newly obtained structural results

673   On the basis of detailed structural analyses, a Main Central Boundary and a D_{1W} top-

674   to-the-N/NW thrusting in the Northwestern Zone are argued for the first time in the

675   LMTB. The Main Central Boundary corresponds to a major tectonic boundary

676   supported both by field structures and geophysical profile (Jia et al., 2006; Robert et al.,

677   2010b), which divides the LMTB into a Northwestern Zone (part of the Songpan–Ganzi

678   Terrane) to the northwest and a Southeastern Zone to the southeast. The Southeastern

679   Zone is characterized by exclusively NW-dipping foliations and associated D_{1E} top-to-

680   the-SE thrusting, while the Northwestern Zone is characterized by exclusively SE-

681   dipping foliations and associated D_{1W} top-to-the-NW thrusting.

682   This study subdivides the Southeastern Zone of the LMTB into four units based on

683   increasing deformation intensities and metamorphic grades from southeast to northwest,

684   namely the Autochthon, Para-autochthon, Allochthon, and Inner Metamorphic Core.

685   This subdivision pattern is revised from the previous one that divided the LMTB into

686 an allochthonous sheet thrust southeastwards on top of the autochthonous Sichuan

687 Foreland Basin (Xu et al., 1992; Burchfiel et al., 1995; Worley and Wilson, 1996).

688   In the Southeastern Zone, a D_2 top-to-the-NW normal faulting that cuts the D_{1E} top-

689 to-the-SE thrusting is recognized along the northwest boundary of the Pengguan and

690 Xuelongbao complexes.

691

692 **5.2 Polyphase deformations along the LMTB**

693   According to the geometric and kinematic features and overprinting relationship,

694 together with ^{40}Ar-^{39}Ar and zircon U–Pb data, which allow us to draw a polyphase

695 deformation sequence of the LMTB.

696   5.2.1 Timing of the D_1 main deformation event

697   Timing of the D_{1W} top-to-the-N/NW thrusting is firstly constrained by the emplaced

698 timing of the syntectonic Mupi pluton at *ca.* 219 Ma (Figure 12). Synkinematic

699 recrystallized white mica of sample CX44 that is involved in the top-to-the-N/NW

700 thrusting yields a weighted mean age of 224.1 ± 1.7 Ma, which places a second age

701 constraint on the D_{1W} top-to-the-N/NW thrusting. This newly obtained argon age is

702 consistent with previously published white mica ^{40}Ar-^{39}Ar ages at *ca.* 237–202 Ma from

703 the northern Northwestern Zone (Figure 12)(Yan et al., 2011; Yan et al., 2018). The

704 fact that the zircon U-Pb age of the Mupi pluton is *ca.* 5 Ma younger than the

705 synkinematic white mica ^{40}Ar-^{39}Ar age may suggest the Mupi pluton emplaced during

706 the late phase of the D_{1W} event. Based on the zircon U–Pb age of syntectonic Mupi

707 pluton and synkinematic white mica ^{40}Ar-^{39}Ar age, we, therefore, suggest that the D_{1W}

708 top-to-the-N/NW thrusting event occurred at *ca.* 224–219 Ma.

709   The D_{1E} top-to-the-SE thrusting within the Southeastern Zone has been constrained

710 in the late Triassic for the following arguments: 1) Field observations and seismic

711 reflection profile revealed that late Jurassic–Cenozoic rocks unconformably overly on

712 intensively folded rocks as young as late Triassic (Figures 2 and 4a–d)(BGMRSP, 1991;

713 Jia et al., 2006); 2) Detailed petrological analyses and in-situ allanite U–Pb dating and

714 biotite $^{40}Ar/^{39}Ar$ dating revealed a *ca.* 204–190 Ma peak metamorphism in the Inner

715 Metamorphic Core that postdates the D_{1E} event (Airaghi et al., 2017a; 2018a; 2018c);

716 3) The ages of the voluminous magmatism intruding the extensively folded Songpan–

717 Ganzi Terrane range between 223 and 200 Ma, which postdates the folding in the

718 Songpan–Ganzi Terrane and the top-to-the-SE thrusting of the LMTB (Figure 12)(Xu

719   et al., 1992; Roger et al., 2004; Harrowfield and Wilson, 2005; Hu et al., 2005; Zhang

720   et al., 2007; de Sigoyer et al., 2014). Thus, the regional D_{1E} top-to-the-SE thrusting was

721   at least activated during the late Triassic, together with the contemporary D_{1W} top-to-

722   the-N/NW thrusting recorded within the Northwestern Zone, both of which compose

723   the *ca.* 224–219 Ma main D_1 double-vergent event.

724   5.2.2 Timing of the D_2 top-to-the-NW normal faulting

725   According to the newly obtained ^{40}Ar-^{39}Ar ages, the timing of the D_2 top-to-the-NW

726   normal faulting occurred along the northwest boundary of the Pengguan (*ca.* 27 Ma)

727   and Xuelongbao (*ca.* 80 Ma) complexes are quite different. The top-to-the-NW/N

728   normal faulting is widespread in an over 300 km long zone along the northern margins

729   of the Danba and Kangding complexes, and the northwest margins of the Baoxing,

730   Wulong, Xuelongbao, Moutuo, Pengguan, and Jiaoziding complexes (Figure

731   12)(Burchfiel et al., 1995; Xu et al., 2008; Tian et al., 2016; Xue et al., 2017). This belt

732   of top-to-the-NW normal faulting has previously been entitled East Tibet Detachment

733   (Figure 12)(Wang et al., 2012b). Timing of the East Tibet Detachment top-to-the-NW

734   normal faulting is different at different localities. Hames and Burchfiel (1993) reported

735   a top-to-the-NW normal faulting and syntectonic metamorphism at *ca.* 25 Ma along the

736   northwest Pengguan complex that is in accordance with the *ca.* 27 Ma top-to-the-NW

737   normal faulting as indicated by sample CX2 (Figure 12).

738   Along the northwest boundary of the Wulong complex and north boundary of the

739   Danba complex, the top-to-the-NW/N normal faulting was constrained to *ca.* 81–47 Ma

740   ($^{40}Ar/^{39}Ar$ dating on metamorphic biotite and white mica; Figure 12)(Zhou et al., 2008;

741   Tian et al., 2016). This phase of the top-to-the-NW normal faulting is recorded along

742   the northwest boundary of the Xuelongbao complex (*ca.* 80 Ma ^{40}Ar-^{39}Ar age of sample

743   CX25) as well.

744   A period of the top-to-the-NW/N normal faulting at *ca.* 166–159 Ma was reported

745   at the northwest boundary of the Jiaoziding and Pengguan complexes, and the north

746   boundary of the Danba complex (Figure 12)(Dirks et al., 1994; Zhou et al., 2008; Li,

747   2009). Whereas, younger ages of *ca.* 122–120 Ma related to the top-to-the-N normal

748   faulting at the north boundary of the Danba complex were reported as well (Figure

749   12)(Xu et al., 2008).

750   In summary, the timing of the top-to-the-NW normal faulting of the East Tibet

751   Detachment are scattered at *ca.* 166–159 Ma (north Danba, northwest Pengguan,

752 northwest Jiaoziding), *ca.* 122–120 Ma (north Danba), *ca.*81–47 Ma (north Danba,

753 northwest Wulong) and *ca.* 27–25 Ma (northwest Pengguan; Figure 12). Nonetheless,

754 a process is required to explain these four groups of well-defined argon plateau ages

755 that do not show an age-changing trend in map view (Figure 12). We, therefore, prefer

756 to interpret that the top-to-the-NW/N normal faulting of the East Tibet Detachment was

757 episodically and co-planarly activated at *ca.* 166–159 Ma, *ca.* 122–120 Ma, *ca.* 81–47

758 Ma, and *ca.* 27–25 Ma (Figure 12). The late-stage activations could partially reset the

759 fine-grained white mica argon system that resulted in stair-shaped spectra yielded by

760 samples of CX18 and CX19 (Figures 11 and 12).

761

762 **5.3 Episodic basement-slice-imbrication and amphibolite facies metamorphic rock**

763 **exhumation**

764 The Western Sichuan Foreland Basin (WSFB) was formed by loading and

765 subsidence due to the southeastward thrusting of the LMTB along the Yingxiu–

766 Beichuan Fault and Xiaoguanzi Fault (T$_2$ in Figure 12)(Chen and Wilson, 1996; Li et

767 al., 2003). Episodic terrestrial deposition in the WSFB from the late Triassic to the

768 present day indicates that the LMTB continued to be tectonically active episodically

769 during the late Triassic to early Jurassic, late Jurassic to early Cretaceous, and late

770 Cretaceous to earliest Paleocene (Figure 12)(Xu et al., 2008; Li et al., 2013c; Tian et

771 al., 2016).

772 The late Jurassic to early Cretaceous southeastward thrusting of the Yingxiu–

773 Beichuan Fault and Xiaoguanzi Fault (T$_2$ in Figure 12), as the southeast boundary Fault

774 of the Pengguan and Baoxing complexes, overlaps the *ca.* 166–159 Ma and *ca.* 122–

775 120 Ma top-to-the-NW/N normal faulting along the NW boundary of the Jiaoziding

776 complex and the north boundary of the Danba complex (Figure 12)(Xu et al., 2008;

777 Zhou et al., 2008; Li, 2009). The late Cretaceous–earliest Paleocene southeastward

778 thrusting of the Yingxiu–Beichuan Fault and Xiaoguanzi Fault is also coeval with the

779 top-to-the-NW/N normal faulting along the NW boundary of the Xuelongbao (CX25

780 in this study) and Wulong (Tian et al., 2016) complexes (Figure 12). Furthermore, both

781 the top-to-the-SE thrusting and top-to-the-NW normal faulting along the southeast and

782 northwest boundaries of the complexes occurred under similar greenschist-facies

783 metamorphic conditions (Airaghi et al., 2017b; Xue et al., 2017). Conjugated

784 kinematics of boundary SE-thrusting and NW-normal faulting characterized by similar

785   metamorphic conditions and synchronous timing let us propose that the Xuelongbao,

786   Pengguan, Baoxing and Wulong complexes were episodically imbricated to the

787   southeast as basement-slices during late Jurassic–early Cretaceous and late Cretaceous–

788   earliest Paleocene.

789   Numerical modeling of co-seismic slip vectors *vs*. fault angles indicates that the

790   latest high-angle listric Yingxiu–Beichuan Fault might have facilitated the vertical

791   imbrication of the Pengguan complex with no need of the SE-ward thrusting and

792   loading (Feng et al., 2015). This feature explains the absence of a rejuvenated foreland

793   basin contemporary to the 27–25 Ma basement imbrication. Nevertheless, the 27–25

794   Ma basement slice imbrication of the Pengguan complex is compatible with its 30–25

795   Ma fast cooling (Figure 12)(Wang et al., 2012a).

796   In the map view, two amphibolite facies metamorphic zones wrap the Xuelongbao

797   and Danba complexes (Figure 13a). Both amphibolite facies metamorphic zones

798   reached peak conditions at *ca*. 210–180 Ma post to the late Triassic orogeny (Figure

799   12)(Dirks et al., 1994; Huang et al., 2003a; Weller et al., 2013; Airaghi et al., 2018a).

800   Gravity anomaly indicated that the Xuelongbao complex probably extends

801   northeastwards beneath and parallel to the amphibolite facies metamorphic rocks (Xue

802   et al., 2017). Coincidently, the Wenchuan–Xuelongbao and Danba amphibolite facies

803   metamorphic zones experienced rapid exhumation and cooling during the late Jurassic

804   to early Cretaceous (CX12 and CX33 in this work) that is coeval with the

805   aforementioned late Jurassic–early Cretaceous basement-slice-imbrication (Figure

806   13b)(Arne et al., 1997; Huang et al., 2003a; Tian et al., 2016; Airaghi et al., 2018a).

807   Both gravity inversion (Xue et al., 2017) and seismic reflection profiles (Guo et al.,

808   2013) revealed a belt of basement-slice hidden right beneath a Mesozoic Laojungou

809   granite (224 ± 5 Ma; Zhao et al., 2007) within the east Songpan–Ganzi Terrane (Figure

810   13a). The Laojungou granite recorded rapid exhumation and cooling during the late

811   Jurassic to early Cretaceous as well (Figure 13b)(Yuan et al., 1991).

812   Considering the spatial–cooling–imbricating relationships between the Laojungou

813   granite, amphibolite facies metamorphic zones and basement-slices, we interpret that

814   the Laojungou granite and amphibolite facies metamorphic rocks were popped up by a

815   basement-slice-imbrication during the late Jurassic–early Cretaceous. The basement-

816   slice-imbrication was responsible for localized fast cooling and exhumation of the

817   amphibolite-facies metamorphic rocks. However, the Wenchuan–Xuelongbao

818 metamorphic sedimentary cover does not show fast cooling during the late Cretaceous–

819 earliest Paleocene and at *ca.* 27–25 Ma comparing to the basement-slice-imbrication

820 (Figure 13b), which needs further work.

821

822 **5.4 Mesozoic tectonic evolution of the LMTB**

823 The Mesozoic tectonic evolution of the LMTB can be summarized as follows

824 without consideration of the top-to-the-N/NW thrusting in the Northwestern Zone.

825 Namely, the Songpan–Ganzi Terrane subducted to the north along the Anymaqen

826 Suture Zone and/or to the southwest along the Jinshajiang Suture Zone, which resulted

827 in the top-to-the-S shearing of the thick Triassic flysch cover along a basal decollement

828 layer (Mattauer et al., 1992; Calassou, 1994) and associated sinistral strike-slip to the

829 southeastward thrusting in the LMTB (Xu et al., 1992; Dirks et al., 1994; Burchfiel et

830 al., 1995; Worley and Wilson, 1996; Roger et al., 2004; Harrowfield and Wilson, 2005).

831 The amphibolite facies metamorphism in the Wenchuan–Xuelongbao area reached the

832 peak pressure of > 11 ± 2 kbar at *ca.* 200 Ma (Airaghi et al., 2018b) required a

833 sedimentary cover more than 30 km in thickness. However, high-resolution seismic

834 reflection and gravity modeling profiles revealed a ~20 km thickness cover of the

835 Songpan–Ganzi Terrane (Guo et al., 2013; Xue et al., 2017) that is far thinner than the

836 required ~30 km thickness.

837 In contrast, Sengör (1984) and Luo (1991) regarded the LMTB as an early Mesozoic

838 intracontinental subduction zone but lack details of structural observation. Considering

839 the pervasive top-to-the-N/NW thrusting in the Northwestern Zone and top-to-the-SE

840 thrusting in the Southeastern Zone, we thus prefer an early Mesozoic intracontinental

841 subduction along the LMTB.

842 In this work, the Main Central Boundary, devoid of ophiolitic rocks separating the

843 Southeastern Zone to the SE from the Northwestern Zone to the NW, does not represent

844 an ophiolitic suture zone, but a tectonic "scar" corresponding to the place where the

845 Yangtze basement was underthrusted. Like the Chenzhou–Linwu Fault in the

846 Xuefengshan Intracontinental Orogen (South China) where the South China Block

847 underthrusted (Chu et al., 2012a; Chu et al., 2012b). Along the LMTB, the

848 underthrusting was coeval with important burial (> 11 ± 2 kbar) and the double-vergent

849 thrusting in both sides of the Main Central Boundary. The basement underthrusting is

850 also supported by the blueschist with intraplate affinity reported along the Qingchuan–

851   Pingwu Fault (Wei, 1994; Xu et al., 2020). A new tectonic scenario is proposed here

852   (Figure 14). In the pre-middle Triassic times, the Longmenshan area along the western

853   Yangtze margin was a failed rift evidenced by radiolarian chert, abyssal deposits, slump

854   structures (Long, 1991; Luo, 1991; Chang, 2000; Li, 2009) and seismic profile (Jia et

855   al., 2006). Accompany with the pre-middle Triassic rifting, a series of NW-dipping syn-

856   depositional normal faults developed in the Longmenshan area that dissected the

857   western Yangtze basement to slices, and the lower crust thinned significantly that

858   resulted in a local "weak zone" in the lower crust (Figure 14a).

859   During the late Triassic, the Yangtze basement underthrusting along the "weak zone"

860   accommodated by inversion of the normal faults, which can be linked to the far-field

861   effect of the Paleotethys' closure (Figure 14b)(Luo, 1991; Chen and Wilson, 1996;

862   Meng et al., 2005; Yan et al., 2019). The sedimentary cover was simultaneously

863   shortened by a top-to-the-SE thrusting and a top-to-the-NW thrusting associated with

864   the main D_1 event (Figure 14b). The domain of the top-to-the-SE thrusting in the

865   Southeastern Zone is larger and more extensive than the top-to-the-NW thrusting in the

866   Northwestern Zone. Similar structures were developed in the north Himalaya where a

867   large domain experienced a top-to-the-S thrusting, compared to a small domain with a

868   top-to-the-N thrusting due to the northward subduction of the India plate (Dewey, 1988;

869   Harrison, 1992). We thus favor an NW-ward basement underthrusting along the LMTB

870   (Figure 14b). The large amount of rift rocks transported southeastwards and overlain

871   the autochthonous foreland basin. In addition, a large volume of rocks was

872   underthrusted to crustal depth deeper than 30 km and metamorphosed, as documented

873   by the *ca*. 210–180 Ma amphibolite-facies metamorphic zone that metamorphosed at a

874   peak pressure of > 11±2 kbar (Figure 12)(Weller et al., 2013; Airaghi et al., 2018a;

875   Airaghi et al., 2018b; Airaghi et al., 2018c).

876   During periods of the late Jurassic–early Cretaceous, late Cretaceous–earliest

877   Paleogene, the accretion of Gondwana-derived Terranes to the southern Eurasia plate

878   had resulted in episodic compression in the Longmenshan area (Dewey, 1988; Xu et

879   al., 1992). We cannot rule out the possible contribution of the 150–140 Ma and 120–

880   105 Ma compression resulted from the westward subduction of the Paleo-Pacific plate

881   subduction (Chu et al., 2019). Under the regional episodic compression, basement-

882   slices represented by the Neoproterozoic complexes along the weak zone of the

883   Yangtze Block, including the Xuelongbao, Moutuo, and Danba complexes,

884   episodically imbricated southeastwards along the inherited faults. Basement-slice-
885   imbrication then exhumed the basement complexes and the amphibolite facies
886   metamorphic rocks as documented by the synchronously fast cooling of the meta-
887   sediments and the basement complexes (Figures 12 and 14d)(Yuan et al., 1991; Arne
888   et al., 1997; Huang et al., 2003b; Weller et al., 2013; Tian et al., 2016). Basement-slice-
889   imbrication also reworked the late Triassic allochthonous–autochthonous LMTB into
890   four subdivisions (Figure 14d).

891

892   **7 Conclusions**

893   Based on structural analysis and previous geophysical profile, we have delineated a
894   Main Central Boundary that separates the Longmenshan Thrust Belt into a Southeastern
895   Zone to the southeast and a Northwestern Zone to the northwest.

896   On the basis of different lithologies, increasing strain intensity and metamorphic
897   grade, the Southeastern Zone is revised into four subdivisions, namely, the Autochthon,
898   Para-autochthon, Allochthon, and Inner Metamorphic Core.

899   The detailed structural analysis allows us recognizing the multiphase deformation of
900   the LMTB. A main D_1 double-vergent thrusting event, characterized by the D_{1E} top-to-
901   the-SE thrusting in the Southeastern Zone and the D_{1W} top-to-the-NW/N thrusting in
902   the Northwestern Zone, has been recognized. The D_{1E} and D_{1W} events were
903   synchronously occurred corresponding to a late Triassic intracontinental underthrusting
904   along a "weak zone" of the LMTB. A D_2 top-to-the-NW normal faulting that cuts the
905   D_{1E} top-to-the-SE thrusting has been recognized along the NW boundary of the
906   basement complexes in the Southeastern Zone.

907   Geochronological constraints obtained from this study and the previously published
908   ones indicate that the main D_1 event occurred at *ca*. 224–219 Ma and the D_2 was
909   episodically activated at *ca*. 166–160 Ma, 141–120 Ma, 81–47 Ma, and 27–25 Ma. The
910   episodically and synchronously activated top-to-the-NW normal faulting and top-to-
911   the-SE thrusting along the northwest and SE boundaries of the basement complexes let
912   us propose that the basement-slices episodically imbricated to the SE during the late
913   Jurassic–early Cretaceous and late Cretaceous–earliest Paleocene. The basement-slice
914   imbrication exhumed the D_1-related amphibolite facies rocks to the subaerial and
915   reworked allochthonous–autochthonous LMTB into a four subdivision one.

916

Figure captions

Figure 1. (a) Simplified tectonic sketch of China. QLDB: Qingling–Dabie Orogenic Belt; EKL–ANMQS: East Kunlun–Anymaqen Suture Zone; JSZ: Jinshajiang Suture Zone; SGT: Songpan–Ganzi Terrane; LMTB: Longmenshan Thrust Belt; ICB: Indochina Block; (b) Simplified geological map of the Longmenshan Thrust Belt, modified after BGMRSP (1991), Burchfiel et al. (1995) and Xu et al. (2008). T_1: Anxian–Guanxian Fault; T_2: Yingxiu–Beichuan Fault; T_3: Wenchuan–Maoxian Fault; T_4: Qingchuan–Pingwu Fault; JZD: Jiaoziding complex; PG: Pengguan complex; XLB: Xuelongbao complex; BX: Baoxing complex; KD: Kangding complex; DB: Danba complex; MT: Moutuo complex; WL: Wulong complex; RLG: Rilonguan granite; LJG: Laojungou granite.

Figure 2. Geological map of the north and middle parts of the LMTB and its adjacent area, modified after BGMRSP (1991) and Xu et al. (2008). MP: Mupi pluton. Symbols and acronyms are the same as in Figure 1.

Figure 3. (a) Structural division, field elements including foliation, lineation, and kinematics of the LMTB. (b-d) π-circle projection of the bedding (S_0) in the Para-autochthon from south to north. All field elements are shown in a lower hemisphere equal-area projection. Symbols and acronyms are the same as in Figure 1.

Figure 4. (a–d) Geological cross-sections perpendicular to the LMTB. Purple solid lines represent the foliations attitude (Locations are marked in Figure 2). Subaerial structures of these cross-sections are based on our field mapping and the deep structures are based on seismic reflection data of Jia et al. (2006) and Guo et al. (2013). The black dashed lines represent speculated folds. (e) Flower structure revealed

950 by the seismic reflection profile processed by Jia et al. (2006)(Location is marked in Figure 4d). MCB:

951 Main Central Boundary; AGF: Anxian–Guanxian Fault; YBF: Yingxiu–Beichuan Fault; WMF:

952 Wenchuan–Maoxian Fault; QCF: Qingchuan–Pingwu Fault. Other symbols and acronyms are the same

953 as in Figure 1

954

955 Figure 5. Rock characteristics and deformation style of the Main Central Boundary. (a) Intensely

956 deformed argillaceous limestone characterized by a vertical foliation [31°34.833' N, 103°24.041' E]. (b)

957 Graphite-bearing pelite was intensely foliated to shale with vertical attitude [31°35.916' N, 103°24.008'

958 E]. (c) Foliated thin-bedded limestone and quartz ribbon interlayer and rootless intra-folial folds coexist

959 with vertical foliation [31°48.403' N, 103°44.080' E]. Rootless folds in figures b–c implying significant

960 shortening. Locations are presented in Figure 3a.

961

962 Figure 6. Structural features related to the Main Deformation (D_{1E}) in the Southeastern Zone. **In the**

963 **Inner Metamorphic Core**: (a) Lineation formed by aligned biotite plunging N335° by 30° on the S-

964 dipping foliation [31°30.359' N, 103°34.123' E]. (b) Asymmetric pyrite pressure shadow indicating a

965 top-to-the-SE thrusting [31°42.210' N, 103°51.067' E]. (c) Sigma-shaped feldspar porphyroclast in

966 paragneiss indicating a top-to-the-SE thrusting [31°05.193' N, 103°18.730' E]. (d) S/C fabric observed

967 under Cross Polarized Light (CPL) indicating a top-to-the-SE thrusting. **In the Allochthon**: (e) Sigmoid

968 pelitic lens and "cold" S/C structures developed in the Neoproterozoic Huangshuihe Group suggesting a

969 to the top-to-the-SE thrusting [31°16.195' N, 103°46.747' E]. (f) Sigma-shaped sandy lens in Silurian

970 pelitic schist within the nappe indicating a top-to-the-SE thrusting [32°04.577' N, 104°40.599' E]. (g) At

971 the rear of the klippe, thick-bedded limestone thrust to the SE along an NW-dipping reverse fault

972 [31°11.530' N, 103°45.929' E]. **In the Para-autochthon**: (h) Sigmoid lens and "cold" S/C fabrics

973 indicating a top-to-the-SE thrusting [30°55.403' N, 103°20.495' E]. Figure locations are marked in Figure

974 3a. X and Z axes are marked on the figures. Mineral abbreviations are after Kretz (1983).

975

976 Figure 7. Structural features related to the Main Deformation (D_{1W}) in the Northwestern Zone. **In the**

977 **northern Northwestern Zone**: (a) Aligned calcite, fine-grained white mica, and oxide-pods define

978 lineation plunging to the south on the S-dipping foliation [32°30.892' N, 104°08.178' E]. (b) Sigma-

979 shaped pebbles in a meta-conglomerate indicating a top-to-the-N sense of shear [32°53.562' N,

980 105°04.820' E]. (c) Deflected quartz ribbon observed under CPL indicating a top-to-the-N thrusting. (d)

981 Asymmetric feldspar porphyroclast wrapped by deflected white mica suggesting a top-to-the-N thrusting.

982 (e) Northward verging chevron fold associated with meter-scale reverse fault indicating a top-to-the-N

983 thrusting [32°25.219' N, 104°31.513' E]. (f) Bedding depicted by compositional banding showing an N-

984 verging fold, and bedding to sub-parallel to the foliation in the limbs [32°228.591' N, 104°26.763' E]. **In**

985 **the southern Northwestern Zone**: (g) Asymmetric garnet pseudomorph pressure shadow suggesting a

986 top-to-the-NW thrusting. (h) Hundred-meter scale chevron fold verging to the NW indicating a top-to-

987 the-NW thrusting [31°33.912' N, 103°16.680' E]. Figure locations are marked in Figure 3a. X and Z axes

988 are marked on the figures. Mineral abbreviations are after Kretz (1983).

989

990 Figure 8. Features of the syn-tectonic Mupi pluton in the Northwestern Zone [32°31.445' N, 104°32.456'

991 E]. (a) Magmatic fabric of the Mupi pluton with euhedral feldspar randomly distributed, about 30 meters

992 north to the south margin of the Mupi pluton. (b) Quartz + feldspar veins parallel to the shear foliation,

993 about 10-15 meters north to the pluton south margin. (c) Strong mylonitisation at the south margin of the

994 pluton shares similar structural geometry and kinematics with the country rock. (d) Asymmetric feldspar

995 porphyroclasts, synthetic offset of feldspar fragments along shear band in XZ plane indicating a top-to-

996 the-N thrusting. (c) Panorama of thin section under CPL of the Mupi pluton, the feldspar brittle cracks

997 (marked by red arrow) infilled by quartz subparallel to the shear foliation. X and Z axes are marked on

998 the figures. Figure locations are marked in Figure 3a. Mineral abbreviations are after Kretz (1983).

999

1000 Figure 9. Structural features related to the top-to-the-NW normal faulting along the northwest boundary

1001 of the Neoproterozoic complexes. (a) At the northwest boundary of the **Xuelongbao complex**, sigmoid

1002 feldspar phenocrysts associated with S/C fabric indicating a top-to-the-NW normal faulting [31°19.683'

1003 N, 103°23.874' E]. At the northwest boundary of the **Pengguan complex**: (b) Granitic mylonite having

1004 foliation dips to the NW [31°22.931' N, 103°30.364' E]. (c–d) Mica fish in the quartz schist (PPL) and

1005 σ-type porphyroclast (CPL) wrapped by deflected micas indicating a top-to-the-NW normal faulting. (e)

1006 Shear-band (white dashed line) distributes from the upper-right corner to the lower-left corner that cuts

1007 the whole thin section indicate a top-to-the-NW normal faulting, CPL. Sigmoid porphyroclast (e),

1008 incipient shear band inclining to the SE (f), and white mica shear-band fabric (g) indicate a top-to-the-

1009 SE thrusting related to D_{1E}. All of them are cut by the white shear band related to the D_2 top-to-the-NW

1010 normal faulting, CPL. Locations are marked in Figure 3a. X and Z axes are marked on the figures.

1011 Mineral abbreviations are after Kretz (1983).

1012

1013 Figure 10. (a) CL images of the representative zircons from the Mupi pluton. The scale bar represents

1014 100 μm. (b) SIMS U–Pb Concordia diagram of zircons of the syntectonic Mupi pluton.

1015

Figure 11. ^{40}Ar-^{39}Ar age spectra of the dated samples. We carried out a two-aliquot analysis of micas from CX6, CX12, and CX19 to exclude the influence of occasional deviation on the stair-case age spectrum, and the two-aliquot results are labeled with the suffix of A and B (*eg.,* CX6A, CX6B, CX12A, CX12B, CX19A, CX19B). Inverse isochron diagrams are presented in Figure S3. ^{40}Ar-^{39}calculation results are

summarized in Table 1, and detailed step-heating results are presented in the supporting information Table S2.

Figure 12. Geochronological constraints compiled from published and this study. Ages are shown by the method used to determine the age (A = Ar/Ar; K = K/Ar; U = U/Pb; F = Fission track) and mineral used (Am = Amphibole; B = biotite; M = Muscovite; Z = zircon; Mn = monazite; I= illite; S = Sericite; Wm = white mica). 1. Li (2009); 2. Yan et al. (2018); 3. Yan et al. (2011); 4. Arne et al. (1997); 5. Airaghi et al. (2017b); 6. Airaghi et al. (2018a); 7. Airaghi et al. (2018b); 8. Airaghi et al. (2018c); 9. Zheng et al. (2016); 10. Yan et al. (2008); 11. Zheng et al. (2014); 12. Tian et al. (2016); 13. Huang et al. (2003a); 14. Weller et al. (2013); 15. Xu et al. (2008); 16. Zhou et al. (2008); 17. Wallis et al. (2003); 18. Zhou et al. (2002); 19. Xia (1993); 20. Xu et al. (1992); 21. Yuan et al. (1991); 22. Hu et al. (2005); 23. Zhao (2007); 24. Kirby et al. (2002); 25. Roger et al. (2004); 26. Zhang et al. (2006a); 27. Yuan et al. (2010); 28. BGMRSP (1991); 29. Li et al. (2013c); 30. Wang et al. (2012a). 31. Hames and Burchfiel (1993). Symbols and acronyms are the same as in Figure 2.

Figure 13. (a) Spatial relationship between the amphibolite facies metamorphic zones and the basement complexes along the peripheries of the Songpan–Ganzi Terrane. Isograd lines are presented in color dashed lines accompany relating mineral abbreviations. Mineral abbreviations are after Kretz (1983) except Liq representing the magmatic zone. Symbols and acronyms are the same as in Figure 12. (b) Compiled cooling histories for the Wenchuan–Xuelongbao amphibolite facies metamorphic belt (WXAB, bold dashed line)(Airaghi et al., 2018a), the Danba amphibolite facies metamorphic belt (DBAB), and migmatite zone (DBM, thin dashed line)(Huang et al., 2003a), and the Mesozoic Laojungou granite (LJG, bold gray line)(Yuan et al., 1991). Gray frames show the three episodes of basement-slice-imbrication at late Jurassic–early Cretaceous, late Cretaceous–Earliest Paleocene, *ca.* 27–25 Ma. The Wenchuan–Xuelongbao and the Danba amphibolite facies metamorphic belt and the Laojungou granite experienced a rapid exhumation and cooling during the late Jurassic to the late Cretaceous, and 27-25 Ma.

Figure 14. A possible Mesozoic tectonic evolutionary scenario of the LMTB and adjacent area. (a) Pre-middle Triassic rifting of the Yangtze Block resulted in crustal thinning and a potential "weak zone" in the future Longmenshan area. (b) During the late Triassic, NW-ward Yangtze basement underthrusting along the "weak zone" resulted in extensive shortening, inversion of syn-depositional normal Fault. The sedimentary rocks were buried to a crustal depth deeper than 30 km. NW- and SE-ward thrusting, and associated nappe belt formed at this time. (c) During the late Triassic to early Jurassic, the underthrusted rocks were metamorphosed. Gradient color from green to dark blue in the Inner Metamorphic Core represents show the low- to high-metamorphic grade. (d) late Jurassic–Miocene, basement-slice episodically imbricated to the SE that exhumed the amphibolite facies metamorphic rocks to the subaerial and reworked the LMTB. Symbols and acronyms are the same as in Figure 2.

Table 1. Summary of ^{40}Ar-^{39}Ar dating results

References

Airaghi, L., Janots, E., Lanari, P., de Sigoyer, J., and Magnin, V., 2018a, Allanite petrochronology in fresh and retrogressed garnet-biotite metapelites from the Longmen Shan (eastern Tibet): Journal of Petrology, p. egy109-egy109, https://doi.org/10.1093/petrology/egy109.

Airaghi, L., Lanari, P., de Sigoyer, J., and Guillot, S., 2017a, Microstructural vs compositional preservation and pseudomorphic replacement of muscovite in deformed metapelites from the Longmen Shan (Sichuan, China): Lithos, v. 282-283, p. 262-280, https://doi.org/10.1016/j.lithos.2017.03.013.

Airaghi, L., Sigoyer, J., Guillot, S., Robert, A., Warren, C. J., and Deldicque, D., 2018b, The Mesozoic along-strike tectono-metamorphic segmentation of Longmen Shan (eastern Tibetan plateau): Tectonics, v. 37, p. 4655-4678, https://doi.org/10.1029/2018TC005005.

Airaghi, L., Sigoyer, J. d., Lanari, P., Guillot, S., Vidal, O., Monié, P., Sautter, B., and Tan, X., 2017b, Total exhumation across the Beichuan fault in the Longmen Shan (eastern Tibetan plateau, China): constraints from petrology and thermobarometry: Journal of Asian Earth Sciences, https://doi.org/10.1016/j.jseaes.2017.04.003.

Airaghi, L., Warren, C. J., de Sigoyer, J., Lanari, P., and Magnin, V., 2018c, Influence of dissolution/reprecipitation reactions on metamorphic greenschist to

amphibolite facies mica 40Ar/39Ar ages in the Longmen Shan (eastern Tibet): Journal of Metamorphic Geology, v. 36, no. 7, p. 933-958, https://doi.org/10.1111/jmg.12420.

Arne, D., Worley, B., Wilson, C., Chen, S. F., Foster, D., Luo, Z. L., Liu, S. G., and Dirks, P., 1997, Differential exhumation in response to episodic thrusting along the eastern margin of the Tibetan Plateau: tectonophysics, v. 280, no. 3, p. 239-256, https://doi.org/10.1016/S0040-1951(97)00040-1.

BGMRSP, 1991, Regional geology of Sichuan Province, Beijing, Geological Publishing House, 730 p.:

Billerot, A., Duchene, S., Vanderhaeghe, O., and de Sigoyer, J., 2017, Gneiss domes of the Danba Metamorphic Complex, Songpan Ganze, eastern Tibet: Journal of Asian Earth Sciences, v. 140, p. 48-74, https://doi.org/10.1016/j.jseaes.2017.03.006.

Burchfiel, B. C., Chen, Z., Liu, Y., and Royden, L. H., 1995, Tectonics of the Longmen Shan and Adjacent Regions, Central China: International Geology Review, v. 37, no. 8, p. 661-735, https://doi.org/10.1080/00206819509465424.

Burchfiel, B. C., Royden, L. H., van der Hilst, R. D., Hager, B. H., Chen, Z., King, R. W., Li, C., Lü, J., Yao, H., and Kirby, E., 2008, A geological and geophysical context for the Wenchuan earthquake of 12 May 2008, Sichuan, People's Republic of China: GSA Today, v. 18, no. 7, p. 4-11, https://doi.org/10.1130/gsatg18a.1.

Calassou, S., 1994, Etude tectonique d'une chaîne de décollement. A- Tectonique triasique et tertiaire de la chaîne de Songpan Garzê(Est Tibet). B- Géométrie et cinématique des déformations dans les prismes d'accrétion sédimentaire: Modélisation analogique.

Chang, E. Z., 2000, Geology and Tectonics of the Songpan-Ganzi Fold Belt, Southwestern China: International Geology Review, v. 42, no. 9, p. 813-831, https://doi.org/10.1080/00206810009465113.

Chen, S., and Wilson, C. J. K., 1996, Emplacement of the Longmen Shan Thrust-Nappe Belt along the eastern margin of the Tibetan Plateau: Journal of Structural Geology, v. 18, no. 4, p. 413-429. (In Chinese with english abstract)

Chen, S., Wilson, C. J. L., Luo, Z., and Deng, Q., 1994, The evolution of the Western Sichuan Foreland Basin, southwestern China: Journal of Asian Earth Sciences,

1115   v. 10, no. 94, p. 159–168, https://doi.org/10.1016/0743-9547(94)90016-7.

1116 Chen, S., Wilson, C. J. L., and Worley, B. A., 1995, Tectonic transition from the

1117   Songpan-Garzê Fold Belt to the Sichuan Basin, south-western China: Basin

1118   Research, v. 7, no. 3, p. 235-253, https://doi.org/10.1111/j.1365-

1119   2117.1995.tb00108.x.

1120 Chu, Y., Faure, M., Lin, W., and Wang, Q., 2012a, Early Mesozoic tectonics of the

1121   South China block: Insights from the Xuefengshan intracontinental orogen:

1122   Journal of Asian Earth Sciences, v. 61, p. 199-220,

1123   https://doi.org/10.1016/j.jseaes.2012.09.029.

1124 Chu, Y., Faure, M., Lin, W., Wang, Q., and Ji, W., 2012b, Tectonics of the Middle

1125   Triassic intracontinental Xuefengshan Belt, South China: new insights from

1126   structural and chronological constraints on the basal décollement zone:

1127   International Journal of Earth Sciences, v. 101, no. 8, p. 2125-2150,

1128   https://doi.org/10.1007/s00531-012-0780-5.

1129 Chu, Y., Lin, W., Faure, M., Xue, Z., Ji, W., and Feng, Z., 2019, Cretaceous Episodic

1130   Extension in the South China Block, East Asia: Evidence From the

1131   Yuechengling Massif of Central South China: Tectonics, v. 38, no. 10, p. 3675-

1132   3702, https://doi.org/10.1029/2019tc005516.

1133 Clark, M. K., and Royden, L. H., 2000, Topographic ooze: Building the eastern margin

1134   of Tibet by lower crustal flow: Geology, v. 28, no. 8, p. 703-706,

1135   https://doi.org/10.1130/0091-7613.

1136 Costa, and Maluski, 1988, Use of the 40Ar-39Ar stepwise heating method for dating

1137   mylonite zones: An example from the St. Barth616my Massif (North Pyrenees,

1138   France). Chemical Geology, v. 72, no. 2, p. 127-144,

1139   https://doi.org/10.1016/0168-9622(88)90061-9.

1140 de Sigoyer, J., Vanderhaeghe, O., Duchêne, S., and Billerot, A., 2014, Generation and

1141   emplacement of Triassic granitoids within the Songpan Ganze accretionary-

1142   orogenic wedge in a context of slab retreat accommodated by tear faulting,

1143   Eastern Tibetan plateau, China: Journal of Asian Earth Sciences, v. 88, p. 192-

1144   216, https://doi.org/10.1016/j.jseaes.2014.01.010.

1145 Dewey, J. F., 1988, The Tectonic Evolution of the Tibetan Plateau: Philosophical

1146   Transactions of the Royal Society of London A Mathematical Physical &

1147   Engineering Sciences, v. 327, no. 1594, p. 379-413,

1148   https://doi.org/10.1098/rsta.1988.0135.

1149 Dirks, P., Wilson, C., Chen, S., Luo, Z., and Liu, S., 1994, Tectonic evolution of the NE
1150   margin of the Tibetan Plateau; evidence from the central Longmen Mountains,
1151   Sichuan Province, China: Journal of Southeast Asian Earth Sciences, v. 9, no. 1,
1152   p. 181-192, https://doi.org/10.1016/0743-9547(94)90074-4.

1153 Druschke, P. A., and Wang, T., 2006, Stratigraphic and UPb SHRIMP Detrital Zircon
1154   Evidence for a Neoproterozoic Continental Arc, Central China: Rodinia
1155   Implications: Journal of Geology, v. 114, no. 5, p. 627-636.

1156 Enkelmann, E., Weislogel, A., Ratschbacher, L., Eide, E., Renno, A., and Wooden, J.,
1157   2007, How was the Triassic Songpan‐Ganzi basin filled? A provenance study:
1158   Tectonics, v. 26, no. 4, https://doi.org/10.1029/2006TC002078.

1159 Feng, S., Zhang, P., Liu, B., Wang, M., Zhu, S., Ran, Y., Wang, W., Zhang, Z., Zheng,
1160   W., and Zheng, D., 2015, Deep crustal deformation of the Longmen Shan,
1161   eastern margin of the Tibetan Plateau, from seismic reflection survey and finite
1162   element modelling: Journal of Geophysical Research: Solid Earth, v. 121, p.
1163   767-787, https://doi.org/10.1002/2015JB012352.

1164 Fleck, R. J., Sutter, J. F., and Elliot, D. H., 1997, Interpretation of discordant 40Ar/39Ar
1165   age-spectra of mesozoic tholeiites from antarctica: Geochimica Et
1166   Cosmochimica Acta, v. 41, no. 1, p. 15-32, https://doi.org/10.1016/0016-
1167   7037(77)90184-3.

1168 Guo, X., Gao, R., Randy Keller, G., Xu, X., Wang, H., and Li, W., 2013, Imaging the
1169   crustal structure beneath the eastern Tibetan Plateau and implications for the
1170   uplift of the Longmen Shan range: Earth and Planetary Science Letters, v. 379,
1171   p. 72-80, https://doi.org/10.1016/j.epsl.2013.08.005.

1172 Hames, W. E., and Burchfiel, B. C., 1993, Laser 40Ar/39Ar dating of Cenozoic,
1173   greenschist-facies shear zones, Longmen Shan, China: Geological Society of
1174   America, v. 25, no. 6, p. A-118, https://doi.org/10.1016/0012-821X(94)00079-
1175   4.

1176 Harrison, T. M., 1992, Raising Tibet: Science, v. 255, no. 5052, p. 1663-1670,
1177   https://doi.org/doi: 10.1126/science.55.5052.1663.

1178 Harrison, T. M., Célérier, J., Aikman, A. B., Hermann, J., and Heizler, M. T., 2009,
1179   Diffusion of 40Ar in muscovite: Geochimica Et Cosmochimica Acta, v. 73, no.
1180   4, p. 1039-1051, https://doi.org/https://doi.org/10.1016/j.gca.2008.09.038.

1181 Harrowfield, M. J., and Wilson, C. J. L., 2005, Indosinian deformation of the Songpan
1182   Garze Fold Belt, northeast Tibetan Plateau: Journal of Structural Geology, v. 27,
1183   no. 1, p. 101-117, https://doi.org/10.1016/j.jsg.2004.06.010.

1184 Hu, J., Meng, Q., Shi, Y., and Qu, H., 2005, SHRIMP U-Pb dating of zircons from
1185   granitoid bodies in the Songpan-Ganzi terrane and its implications: Acta
1186   Petrologica Sinica, v. 21, no. 3, p. 867-880. (In Chinese with english abstract)

1187 Huang, M., Maas, R., Buick, I. S., and Williams, I. S., 2003a, Crustal response to
1188   continental collisions between the Tibet, Indian, South China and North China
1189   Blocks: geochronological constraints from the Songpan-Garzê Orogenic Belt,
1190   western China: Journal of Metamorphic Geology, v. 21, no. 3, p. 223-240,
1191   https://doi.org/10.1046/j.1525-1314.2003.00438.x.

1192 Huang, M. H., Buick, I. S., Hou, L. W., Huang, M. H., and Hou, L. W., 2003b,
1193   Tectonometamorphic evolution of the eastern Tibet plateau: Evidence from the
1194   central Songpan-Garze orogenic belt, western China: Journal of Petrology, v.
1195   44, no. 2, p. 255-278, https://doi.org/10.1093/petrology/44.2.255.

1196 Hubbard, J., and Shaw, J. H., 2009, Uplift of the Longmen Shan and Tibetan plateau,
1197   and the 2008 Wenchuan (M = 7.9) earthquake: Nature, v. 458, no. 7235, p. 194-
1198   197, https://doi.org/10.1038/nature07837.

1199 Jia, D., Wei, G., Chen, Z., Li, B., Zeng, Q., and Yang, G., 2006, Longmen Shan fold-
1200   thrust belt and its relation to the western Sichuan Basin in central China: New
1201   insights from hydrocarbon exploration: AAPG bulletin, v. 90, no. 9, p. 1425-
1202   1447, https://doi.org/10.1306/03230605076.

1203 Kirby, E., Reiners, P. W., Krol, M. A., Whipple, K. X., Hodges, K. V., Farley, K. A.,
1204   Tang, W., and Chen, Z., 2002, Late Cenozoic evolution of the eastern margin of
1205   the Tibetan Plateau: Inferences from 40Ar/39Ar and (U - Th)/He
1206   thermochronology: Tectonics, v. 21, no. 1, p. 1-1-1-20,
1207   https://doi.org/10.1029/2000TC001246.

1208 Kretz, R., 1983, Symbols for rock-forming minerals: Amer Miner, v. 68, no. 1, p. 277-
1209   279, https://doi.org/10.1016/0040-1951(84)90122-7.

1210 Lee, J.-Y., Marti, K., Severinghaus, J. P., Kawamura, K., Yoo, H.-S., Lee, J. B., and
1211   Kim, J. S., 2006, A redetermination of the isotopic abundances of atmospheric
1212   Ar: Geochimica et Cosmochimica Acta, v. 70, no. 17, p. 4507-4512,
1213   https://doi.org/10.1016/j.gca.2006.06.1563.

1214 Li, H., Wang, H., Xu, Z., Si, J., Pei, J., Li, T., Huang, Y., Song, S.-R., Kuo, L.-W., Sun,
1215   Z., Chevalier, M.-L., and Liu, D., 2013a, Characteristics of the fault-related
1216   rocks, fault zones and the principal slip zone in the Wenchuan Earthquake Fault
1217   Scientific Drilling Project Hole-1 (WFSD-1): Tectonophysics, v. 584, p. 23-42,
1218   https://doi.org/10.1016/j.tecto.2012.08.021.

1219 Li, H., Wang, H., Yang, G., Xu, Z., Li, T., Si, J., Sun, Z., Huang, Y., Chevalier, M.-L.,
1220   Zhang, W., and Zhang, J., 2015, Lithological and structural characterization of
1221   the Longmen Shan fault belt from the 3rd hole of the Wenchuan Earthquake
1222   Fault Scientific Drilling project (WFSD-3): International Journal of Earth
1223   Sciences, https://doi.org/10.1007/s00531-015-1285-9.

1224 Li, X. H., Liu, Y., Li, Q. L., Guo, C. H., and Chamberlain, K. R., 2009, Precise
1225   determination of Phanerozoic zircon Pb/Pb age by multicollector SIMS without
1226   external standardization: Geochemistry, Geophysics, Geosystems, v. 10, no. 4,
1227   https://doi.org/10.1029/2009gc002400.

1228 Li, X. H., Tang, G. Q., Gong, B., Yang, Y. H., Hou, K. J., Hu, Z. C., Li, Q. L., Liu, Y.,
1229   and Li, W. X., 2013b, Qinghu zircon: A working reference for microbeam
1230   analysis of U-Pb age and Hf and O isotopes: Chinese Science Bulletin, v. 58,
1231   no. 36, p. 4647-4654, https://doi.org/10.1007/s11434-013-5932-x.

1232 Li, Y., Allen, P. A., Densmore, A. L., and Xu, Q., 2003, Evolution of the Longmen Shan
1233   foreland basin (western Sichuan, China) during the Late Triassic Indosinian
1234   orogeny: Basin Research, v. 15, no. 1, p. 117-138,
1235   https://doi.org/10.1046/j.1365-2117.2003.00197.x.

1236 Li, Y., Su, D., Zhou, R., Li, H., Densmore, A. L., Yan, L., and Yan, Z., 2013c, Episodic
1237   orogeny deduced from coeval sedimentary sequences in the foreland basin and
1238   its implication for uplift process of Longmen Mountain, China: Journal of
1239   Mountain Science, v. 10, no. 1, p. 29-42, https://doi.org/10.1007/s11629-013-
1240   2238-z.

1241 Li, Z., 2009, Composition, structural characteristics and evolution of back-
1242   Longmenshan orogen (north section) in the northwest margin of Yangtze block
1243   [Doctoral thesis: Chang'an University, 211 p.

1244 Lin, A., Rao, G., and Yan, B., 2014, Structural analysis of the right-lateral strike-slip
1245   Qingchuan fault, northeastern segment of the Longmen Shan thrust belt, central
1246   China: Journal of Structural Geology, v. 68, p. 227-244,

1247   https://doi.org/10.1016/j.jsg.2014.09.014.

1248 Liu, H., Yan, D., and Wei, G., 2008, Deformation and metamorphism sequence of bikou
1249   terrane in the northwest margin of yangtze plate：implications for extension
1250   collapse and transition of songpan—garze orogenic belt: Acta Geologica Sinica,
1251   no. 04, p. 464-474+578-579. (In Chinese with english abstract)

1252 Long, X., 1991, Several questions of geochronic evolution in the mid-northeast
1253   segment of lLongmenshan Mountains: Journal of Chengdu College of geology,
1254   v. 18, no. 1, p. 8-16. (In Chinese with english abstract)

1255 Lovera, O. M., Richter, F. M., and Harrison, T. M., 1989, 40Ar/39Ar geothermometry
1256   for slowly cooled samples having a distribution of diffusion domain size:
1257   Journal of Geophysical Research, v. 94, no. 17, p. 917-936,
1258   https://doi.org/10.1029/JB094iB12p17917.

1259 Ludwig, K. R., 2003, User's manual for Isoplot 3.00: a geochronological toolkit for
1260   Microsoft Excel: Berkeley Geochrongol. Center Special Publication, v. 4, p. 47–
1261   93.

1262 Luo, Z., 1991, The dynamical model of the lithospheric evolution in Longmenshan
1263   Orogenic Belt: Journal of Chengdu College of geology, no. 1, p. 1-7. (In Chinese
1264   with english abstract)

1265 Ma, Y., Wang, G., and Hu, X., 1996, Tectonic deformation of Pengguan complex: Acta
1266   Geologica Sichuan, no. 02, p. 110-114. (In Chinese with english abstract)

1267 Mattauer, M., Malavieille, J., Calassou, S., Lancelot, J., Roger, R., Hao, Z., Xu, Z. Q.,
1268   and Hou, L. W., 1992, Le chaine Triassique de Songpan-Garze (Ouest Sichuan
1269   et est Tibet): Une chaine de plissement-decollement sur marge passive: Comptes
1270   Rendus de L'Academie Des Sciences, p. 619-626.

1271 McDougall, I., and Harrison, T. M., 1988, Geochronology and thermo- chronology by
1272   the 40Ar/39Ar method, New York, Oxford University Press.

1273 Meng, Q.-R., Wang, E., and Hu, J.-M., 2005, Mesozoic sedimentary evolution of the
1274   northwest Sichuan basin: Implication for continued clockwise rotation of the
1275   South China block: Geological Society of America Bulletin, v. 117, no. 3-4, p.
1276   396-410, https://doi.org/10.1130/B25407.1.

1277 Paterson, S. R., Tobisch, O. T., and Bhattacharyya, T., 1989, Regional, structural and
1278   strain analyses of terranes in the Western Metamorphic Belt, Central Sierra
1279   Nevada, California: Journal of structural geology, v. 11, no. 3, p. 255-273,

1280   https://doi.org/10.1016/0191-8141(89)90066-7.

1281 Phillips, D., Matchan, E. L., Honda, M., and Kuiper, K. F., 2017, Astronomical
1282   calibration of 40 Ar/ 39 Ar reference minerals using high-precision, multi-
1283   collector (ARGUSVI) mass spectrometry: Geochimica et Cosmochimica Acta,
1284   v. 196, p. 351-369, https://doi.org/10.1016/j.gca.2016.09.027.

1285 Richardson, N. J., Densmore, A. L., Seward, D., Fowler, A., Wipf, M., Ellis, M. A.,
1286   Yong, L., and Zhang, Y., 2008, Extraordinary denudation in the Sichuan Basin:
1287   Insights from low-temperature thermochronology adjacent to the eastern margin
1288   of the Tibetan Plateau: Journal of Geophysical Research, v. 113, no. B4,
1289   https://doi.org/10.1029/2006jb004739.

1290 Robert, A., Pubellier, M., De Sigoyer, J., Vergne, J., Lahfid, A., Cattin, R., Findling, N.,
1291   and Zhu, J., 2010a, Structural and thermal characters of the Longmen Shan
1292   (Sichuan, China): tectonophysics, v. 491, no. 1, p. 165-173,
1293   https://doi.org/10.1016/j.tecto.2010.03.018.

1294 Robert, A., Zhu, J., Vergne, J., Cattin, R., Chan, L. S., Wittlinger, G., Herquel, G., de
1295   Sigoyer, J., Pubellier, M., and Zhu, L. D., 2010b, Crustal structures in the area
1296   of the 2008 Sichuan earthquake from seismologic and gravimetric data:
1297   Tectonophysics, v. 491, no. 1-4, p. 205-210,
1298   https://doi.org/10.1016/j.tecto.2009.11.010.

1299 Roger, F., Jolivet, M., Cattin, R., and Malavieille, J., 2011, Mesozoic-Cenozoic
1300   tectonothermal evolution of the eastern part of the Tibetan Plateau (Songpan-
1301   Garze, Longmen Shan area): insights from thermochronological data and
1302   simple thermal modelling: Geological Society, London, Special Publications, v.
1303   353, no. 1, p. 9-25, https://doi.org/10.1144/sp353.2.

1304 Roger, F., Malavieille, J., Leloup, P. H., Calassou, S., and Xu, Z., 2004, Timing of
1305   granite emplacement and cooling in the Songpan–Garzê Fold Belt (eastern
1306   Tibetan Plateau) with tectonic implications: Journal of Asian Earth Sciences, v.
1307   22, no. 5, p. 465-481, https://doi.org/10.1016/s1367-9120(03)00089-0.

1308 Royden, L. H., Burchfiel, B. C., and van der Hilst, R. D., 2008, The geological
1309   evolution of the Tibetan Plateau: science, v. 321, no. 5892, p. 1054-1058,
1310   https://doi.org/10.1126/science.1155371.

1311 Sengör, A. M. C., 1984, The Cimmeride Orogenic System and the Tectonics of Eurasia:
1312   Geological Society of America Special Papers, v. 195, p. 1-74,

1313   https://doi.org/10.1130/SPE195-p1.

1314 Shen, Z.-K., Sun, J., Zhang, P., Wan, Y., Wang, M., Bürgmann, R., Zeng, Y., Gan, W.,
1315   Liao, H., and Wang, Q., 2009, Slip maxima at fault junctions and rupturing of
1316   barriers during the 2008 Wenchuan earthquake: Nature Geoscience, v. 2, no. 10,
1317   p. 718-724, https://doi.org/10.1038/ngeo636.

1318 Sláma, J., Košler, J., Condon, D. J., Crowley, J. L., Gerdes, A., Hanchar, J. M.,
1319   Horstwood, M. S. A., Morris, G. A., Nasdala, L., Norberg, N., Schaltegger, U.,
1320   Schoene, B., Tubrett, M. N., and Whitehouse, M. J., 2008, Plešovice zircon —
1321   A new natural reference material for U–Pb and Hf isotopic microanalysis:
1322   Chemical Geology, v. 249, no. 1, p. 1-35,
1323   https://doi.org/10.1016/j.chemgeo.2007.11.005.

1324 Stacey, J. S., and Kramers, J. D., 1975, Approximation of terrestrial lead isotope
1325   evolution by a two-stage model: Earth and Planetary Science Letters, v. 26, no.
1326   2, p. 207-221, https://doi.org/10.1016/0012-821X(75)90088-6.

1327 Tian, Y., Kohn, B. P., Phillips, D., Hu, S., Gleadow, A. J., and Carter, A., 2016, Late
1328   Cretaceous–earliest Paleogene deformation in the Longmen Shan fold-and-
1329   thrust belt, eastern Tibetan Plateau margin: Pre-Cenozoic thickened crust?:
1330   Tectonics, p. 1-20, https://doi.org/10.1002/2016TC004182.

1331 Wallis, S. R., Tsujimori, T., Aoya, M., Kawakami, T., Terada, K., Suzuki, K., and Hyodo,
1332   H., Cenozoic and Mesozoic metamorphism in the Longmenshan orogen:
1333   Implications for geodynamic models of eastern Tibet, *in* Proceedings AGU Fall
1334   Meeting Abstracts2003, p. 745-748.

1335 Wang, E., Kirby, E., Furlong, K. P., van Soest, M., Xu, G., Shi, X., Kamp, P. J. J., and
1336   Hodges, K. V., 2012a, Two-phase growth of high topography in eastern Tibet
1337   during the Cenozoic: Nature Geosci, v. 5, no. 9, p. 640-645,
1338   https://doi.org/10.1038/ngeo1538.

1339 Wang, E., Meng, K., Chu, J. J., Wang, G., and Chen, Z., East Tibet Detachment:
1340   Evidence for the uplift mechanism of the Longmen Shan fault belt2012b.

1341 Wang, Q., Liang, B., Xie, Q., and He, W., 2000, Research on microstructures and
1342   deformation conditions of the Qingchuan fault zone: Journal of Mineral
1343   Petrology, v. 87, no. 01, p. 87-90. (In Chinese with english abstract)

1344 Wei, C., 1994, Metamorphism and its geological significance of the Bikou Group in the
1345   Shanxi–Gansu–Sichuan border region: Acta Geologica Sinica, v. 68, no. 03, p.

241-254. (In Chinese with english abstact)

Weislogel, A. L., Graham, S. A., Chang, E. Z., Wooden, J. L., and Gehrels, G. E., 2010, Detrital zircon provenance from three turbidite depocenters of the Middle-Upper Triassic Songpan-Ganzi complex, central China: Record of collisional tectonics, erosional exhumation, and sediment production: Geological Society of America Bulletin, v. 122, no. 11-12, p. 2041-2062, https://doi.org/10.1130/b26606.1.

Weller, O. M., St-Onge, M. R., Waters, D. J., Rayner, N., Searle, M. P., Chung, S. L., Palin, R. M., Lee, Y. H., and Xu, X., 2013, Quantifying Barrovian metamorphism in the Danba Structural Culmination of eastern Tibet: Journal of Metamorphic Geology, v. 31, no. 9, p. 909-935, https://doi.org/10.1111/jmg.12050.

West, D. P., and Lux, D. R., 1993, Dating mylonitic deformation by the 40Ar-39Ar method: An example from the Norumbega Fault Zone, Maine: Earth and Planetary Science Letters, v. 120, no. 3-4, p. 221-237, https://doi.org/10.1016/0012-821X(93)90241-Z.

Worley, B. A., and Wilson, C. J., 1996, Deformation partitioning and foliation reactivation during transpressional orogenesis, an example from the Central Longmen Shan, China: Journal of Structural Geology, v. 18, no. 4, p. 395-411, https://doi.org/10.1016/0191-8141(95)00095-U.

Xia, Z., 1993, Syntectonic regional epimetamorphism of the Triassic terrigenous detrital rocks in the Songpan-Ganze orogneic belt during the early Yanshanian orogney: Acta Geologica Sichuan, no. 03, p. 189-192. (In Chinese with english abstract)

Xu, C., Wells, M. L., Yan, D.-P., Qiu, L., Zhou, Y., and Zhang, Y., 2020, Phase equilibria and geochronology of Triassic blueschists in the Bikou terrane and Mesozoic tectonic evolution of the northwestern margin of the Yangtze Block (SW China): Journal of Asian Earth Sciences, v. 201, p. 104513, https://doi.org/https://doi.org/10.1016/j.jseaes.2020.104513.

Xu, Z., Hou, L., and Wang, Z., 1992, Orogenic process of the Songpan-Ganzé Orogenic belt of China., Geological Publishing House, Beijing, 1-189 p.:

Xu, Z., Ji, S., Li, H., Hou, L., Fu, X., and Cai, Z., 2008, Uplift of the Longmen Shan range and the Wenchuan earthquake: Episodes, v. 31, no. 3, p. 291-301,

https://doi.org/10.1007/s00254-008-1393-y.

Xue, Z., Martelet, G., Lin, W., Faure, M., Chen, Y., Wei, W., Li, S., and Wang, Q., 2017, Mesozoic crustal thickening of the Longmenshan belt (NE Tibet, China) by imbrication of basement slices: insights from structural analysis, petrofabric and magnetic fabric studies, and gravity modeling: Tectonics, p. 3110-3134, https://doi.org/10.1002/2017TC004754.

Xue, Z., Shang, Q., Jiang, W., Wang, Q., and Li, S., 2016, Emplacement age and tectonic implications of the brecciated limestone at the edge of the Longmenshan klippe: Science China Earth Sciences, v. 59, no. 3, p. 590-600, https://doi.org/10.1007/s11430-015-5209-0.

Yan, D., Zhou, M., Li, S., and Wei, G., 2011, Structural and geochronological constraints on the Mesozoic‐Cenozoic tectonic evolution of the Longmen Shan thrust belt, eastern Tibetan Plateau: Tectonics, v. 30, no. 6, p. 1-24, https://doi.org/10.1029/2011TC002867.

Yan, D., Zhou, M., Wei, G., Gao, J., Liu, S., Xu, P., and Shi, X., 2008, The Pengguan tectonic dome of Longmen Mountains, Sichuan Province: Mesozoic denudation of a Neoproterozoic magmatic arc-basin system: Science in China Series D: Earth Sciences, v. 51, no. 11, p. 1545-1559, https://doi.org/10.1007/s11430-008-0126-0.

Yan, D.-P., Qiu, L., Wells, M. L., Zhou, M.-F., Meng, X., Lu, S., Zhang, S., Wang, Y., and Li, S.-B., 2018, Structural and Geochronological Constraints on the Early Mesozoic North Longmen Shan Thrust Belt: Foreland Fold-Thrust Propagation of the SW Qinling Orogenic Belt, Northeastern Tibetan Plateau: Tectonics, v. 37, no. 12, p. 4595-4624, https://doi.org/10.1029/2018tc004986.

Yan, Q., Wang, Z., Hanson, A., Druschke, P., Yan, Z., Liu, D., Jian, P., Song, B., Wang, T., and Jiang, C., 2003, SHRIMP age and geochemistry of the Bikou volcanic terrane: implications for Neoproterozoic tectonics on the northern margin of the Yangtze Craton: Acta Geologica Sinica (English Edition), v. 77, no. 4, p. 479-490.

Yan, Z., Tian, Y., Li, R., Vermeesch, P., Sun, X., Li, Y., Rittner, M., Carter, A., Shao, C., Huang, H., and Ji, X., 2019, Late Triassic tectonic inversion in the upper Yangtze Block: Insights from detrital zircon U–Pb geochronology from south-western Sichuan Basin: Basin Research, v. 31, no. 1, p. 92-113,

https://doi.org/https://doi.org/10.1111/bre.12310.

Yin, A., The Songpan-ganzi terrane of Tibet: was it a part of South China since the Neopreoterozoic, *in* Proceedings 2015 GSA Annual Meeting in Baltimore, Maryland, USA, 2015, Volume 47, Geological Society of America, p. 38.

Yin, A., and Nie, S., 1993, An indentation model for the North and South China collision and the development of the Tan-Lu and Honam fault systems, Eastern Asia: Tectonics, v. 12, no. 4, p. 801-813.

Yuan, C., Zhou, M.-F., Sun, M., Zhao, Y., Wilde, S., Long, X., and Yan, D., 2010, Triassic granitoids in the eastern Songpan Ganzi Fold Belt, SW China: Magmatic response to geodynamics of the deep lithosphere: Earth and Planetary Science Letters, v. 290, no. 3-4, p. 481-492, https://doi.org/10.1016/j.epsl.2010.01.005.

Yuan, H., Zhang, Z., and Zhang, P., 1991, The uplift and cooling histories of Laojungou granite in the western margin of the central Longmen Mountain: Journal of Chengdu College of geology, v. 18, no. 1, p. 17-22. (In Chinese with english abstract)

Zhang, H., Parrish, R., Zhang, L., Xu, W., Yuan, H., Gao, S., and Crowley, Q. G., 2007, A-type granite and adakitic magmatism association in Songpan–Garze fold belt, eastern Tibetan Plateau: Implication for lithospheric delamination: Lithos, v. 97, no. 3-4, p. 323-335, https://doi.org/10.1016/j.lithos.2007.01.002.

Zhang, H., Zhang, L., Harris, N., Jin, L., and Yuan, H., 2006a, U–Pb zircon ages, geochemical and isotopic compositions of granitoids in Songpan-Garze fold belt, eastern Tibetan Plateau: constraints on petrogenesis and tectonic evolution of the basement: Contributions to Mineralogy and Petrology, v. 152, no. 1, p. 75-88, https://doi.org/10.1007/s00410-006-0095-2.

Zhang, H.-P., Liu, S.-F., Yang, N., Zhang, Y.-Q., and Zhang, G.-W., 2006b, Geomorphic characteristics of the Minjiang drainage basin (eastern Tibetan Plateau) and its tectonic implications: New insights from a digital elevation model study: The Island Arc, v. 15, no. 2, p. 239-250, https://doi.org/10.1111/j.1440-1738.2006.00524.x.

Zhang, K.-J., Li, B., Wei, Q.-G., Cai, J.-X., and Zhang, Y.-X., 2008, Proximal provenance of the western Songpan–Ganzi turbidite complex (Late Triassic, eastern Tibetan plateau): Implications for the tectonic amalgamation of China:

Sedimentary Geology, v. 208, no. 1-2, p. 36-44, https://doi.org/10.1016/j.sedgeo.2008.04.008.

Zhang, P., Shen, Z., Wang, M., Gan, W., Bürgmann, R., Molnar, P., Wang, Q., Niu, Z., Sun, J., Wu, J., Hanrong, S., and Xinzhao, Y., 2004, Continuous deformation of the Tibetan Plateau from global positioning system data: Geology, v. 32, no. 9, p. 809, https://doi.org/10.1130/g20554.1.

Zhang, Y. X., Li, B., Wei, Q. G., Wang, Y., and Zhang, K. J., 2006c, Detrital zircon provenance of the Late Triassic Songpan-Ganzi complex: Sedimentary record of collision of the North and South China blocks: Comment and Reply: COMMENT: Geology, v. 34, no. 1, p. e107-e107, https://doi.org/10.1130/g22944.1.

Zhang, Z., Wang, Y., Chen, Y., Houseman, G. A., Tian, X., Wang, E., and Teng, J., 2009, Crustal structure across Longmenshan fault belt from passive source seismic profiling: Geophysical Research Letters, v. 36, no. 17, p. L17310-, https://doi.org/10.1029/2009gl039580.

Zhang, Z., Yuan, X., Chen, Y., Tian, X., Kind, R., Li, X., and Teng, J., 2010, Seismic signature of the collision between the east Tibetan escape flow and the Sichuan Basin: Earth and Planetary Science Letters, v. 292, no. 3-4, p. 254-264, https://doi.org/10.1016/j.epsl.2010.01.046.

Zhao, Y., 2007, Mesozoic granitoids in Eastern Songpan-Garze: Geochemistry, petrogenesis and tectonic implications [Doctor: Graduate school of the Chinese Academy of Sciences, 111 p.

Zheng, Y., Kong, P., and Fu, B., 2014, Time constraints on the emplacement of klippen in the Longmen Shan thrust belt and tectonic implications: Tectonophysics, v. 634, p. 44-54, https://doi.org/10.1016/j.tecto.2014.07.018.

Zheng, Y., Li, H., Sun, Z., Wang, H., Zhang, J., Li, C., and Cao, Y., 2016, New geochronology constraints on timing and depth of the ancient earthquakes along the Longmen Shan fault belt, eastern Tibet: Tectonics, v. 35, no. 12, p. 2781-2806, https://doi.org/10.1002/2016TC004210.

Zhou, M., Yan, D., Kennedy, A. K., Li, Y., and Ding, J., 2002, SHRIMP U–Pb zircon geochronological and geochemical evidence for Neoproterozoic arc-magmatism along the western margin of the Yangtze Block, South China: Earth and Planetary Science Letters, v. 196, no. 1, p. 51-67,

1478   https://doi.org/10.1016/S0012-821X(01)00595-7.

1479 Zhou, M., Yan, D., Vasconcelos, P. M., Li, J., and Hu, R., 2008, Structural and

1480   geochronological constraints on the tectono-thermal evolution of the Danba

1481   domal terrane, eastern margin of the Tibetan plateau: Journal of Asian Earth

1482   Sciences, v. 33, no. 5, p. 414-427, https://doi.org/10.1002/2016TC004210.

1483

Figure 1

Figure 2

Rock units

- Cenozoic
- Cretaceous
- Jurassic
- Middle Triassic–Late Triassic
- Devonian - Early Triassic
- Silurian
- Sinian–Ordovician
- Proterozoic
- Mesozoic granites
- Proterozoic granites

Structures

- Main Central Boundary
- Detected/inferred thrust
- Normal fault
- Overturned bedding
- Overturned bedding from BGMRSP 1991
- Foliation and lineation
- Bedding
- Klippe
- Unconformity

0   km   20

Figure 3

Figure 4

Figure 5

Figure 6

(a) Inner metamorphic core — N335° — 5cm

(b) SE — NW — Inner metamorphic core — 2mm

(c) NW — SE — Inner metamorphic core — 1cm

(d) SE — NW — Compaction plane (S) — Shear plane (C) — Wm — CX6 — Inner metamorphic core — 200μm

(e) NW — SE — Allochthon–nappe — 1 m

(f) NW — SE — Allochthon–nappe — 2 cm

(g) NW — SE — Thick-bedded limestone — Thick-bedded limestone — Allochthon–klippe — 10cm

(h) SE — NW — Para-autochthon — 1cm
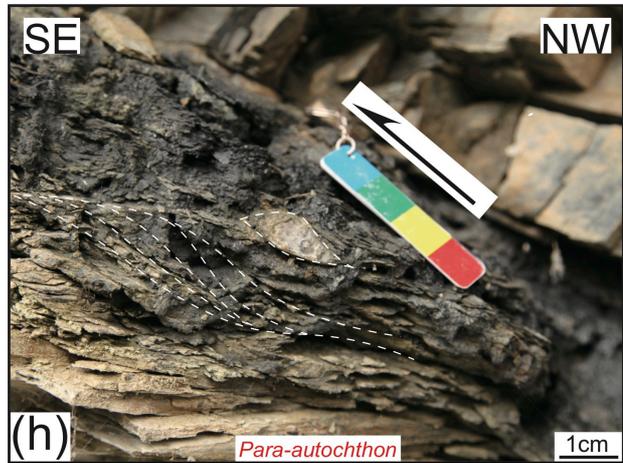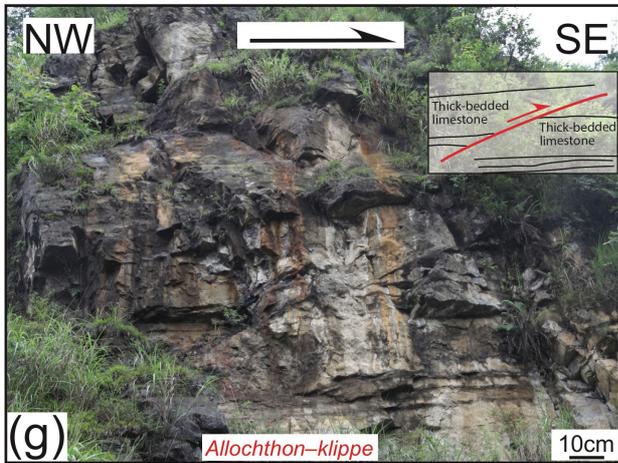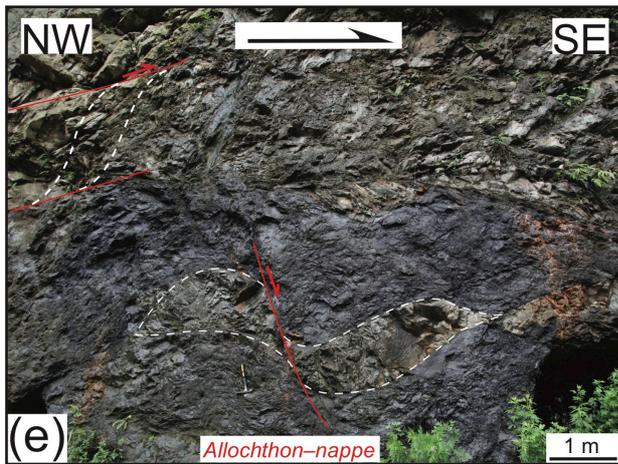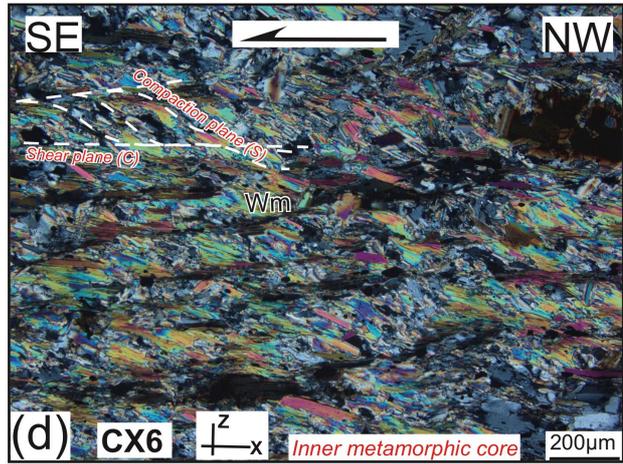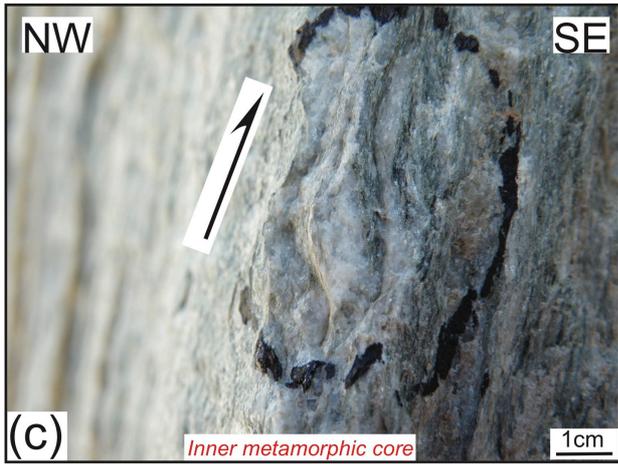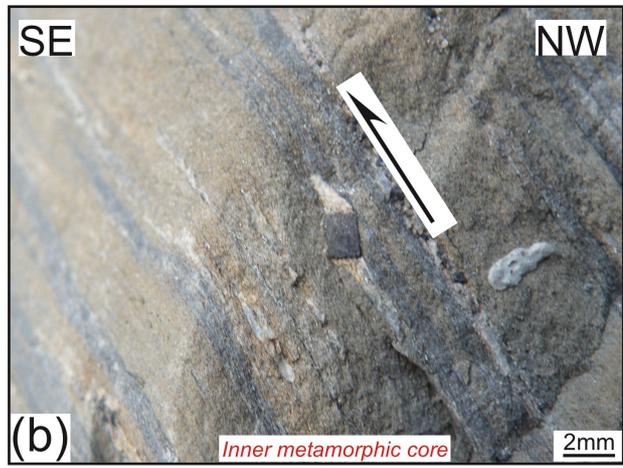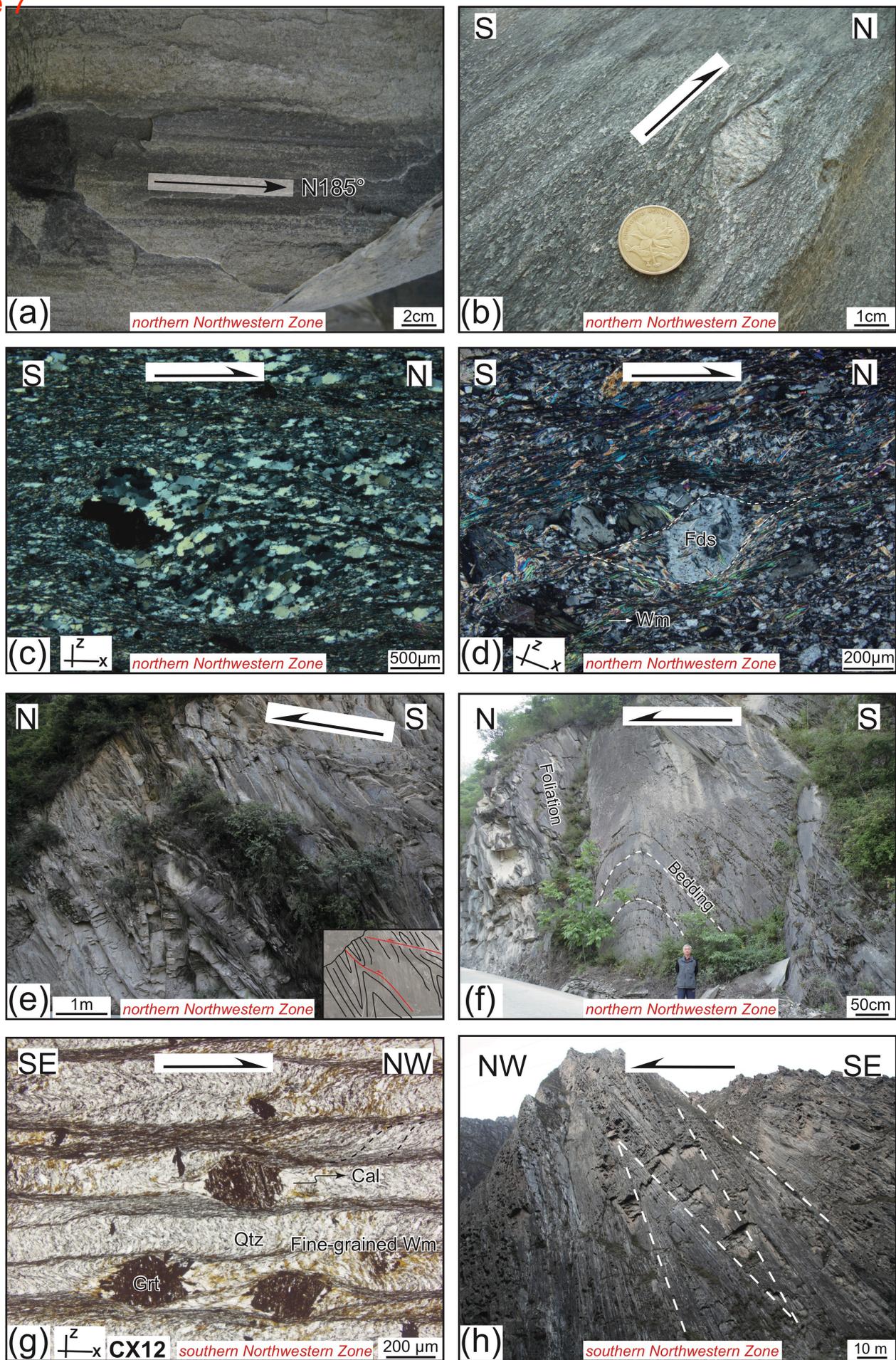
Figure 7

Figure 8

~30 meters north to the south
margin of the Mupi pluton
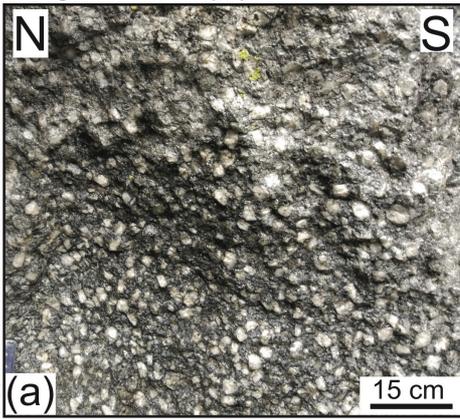
N   S

(a)   15 cm

~10–15 meters north to the south
margin of the Mupi pluton

N   S

Qtz+Fds vein

(b)   50 cm

South margin of the Mupi pluton

N   S

(c)   2 cm

N   S

Fds

(d)   1 cm

Foliation

Fds

Qtz

(e)   2 mm
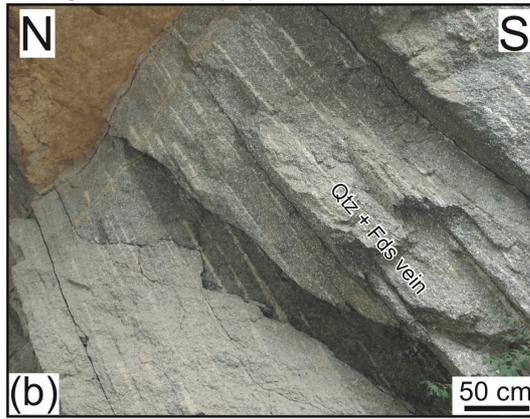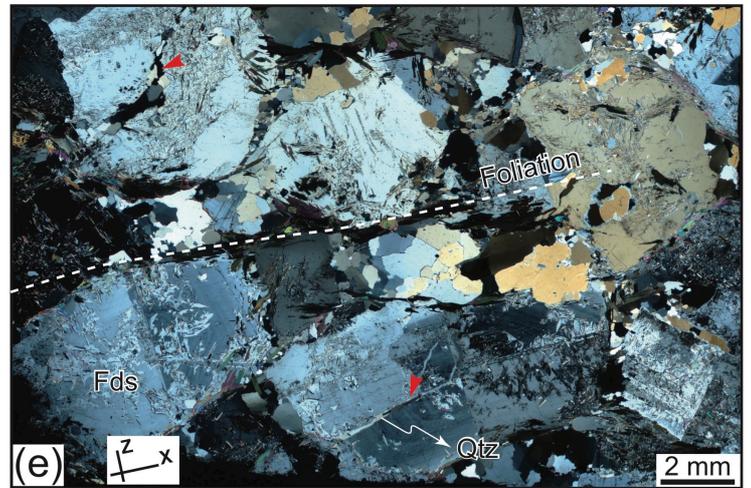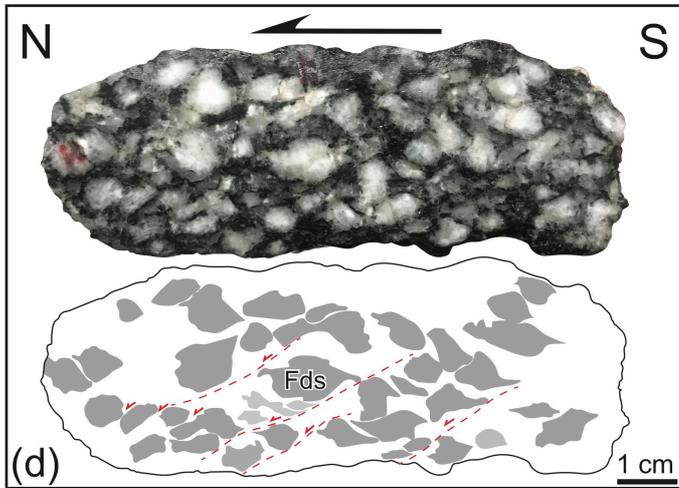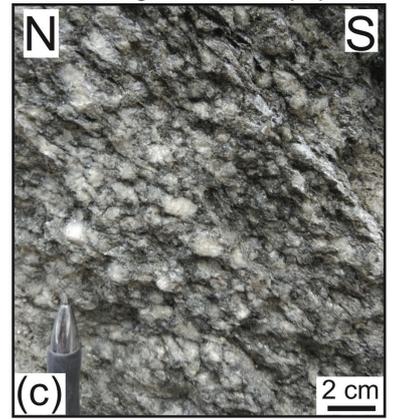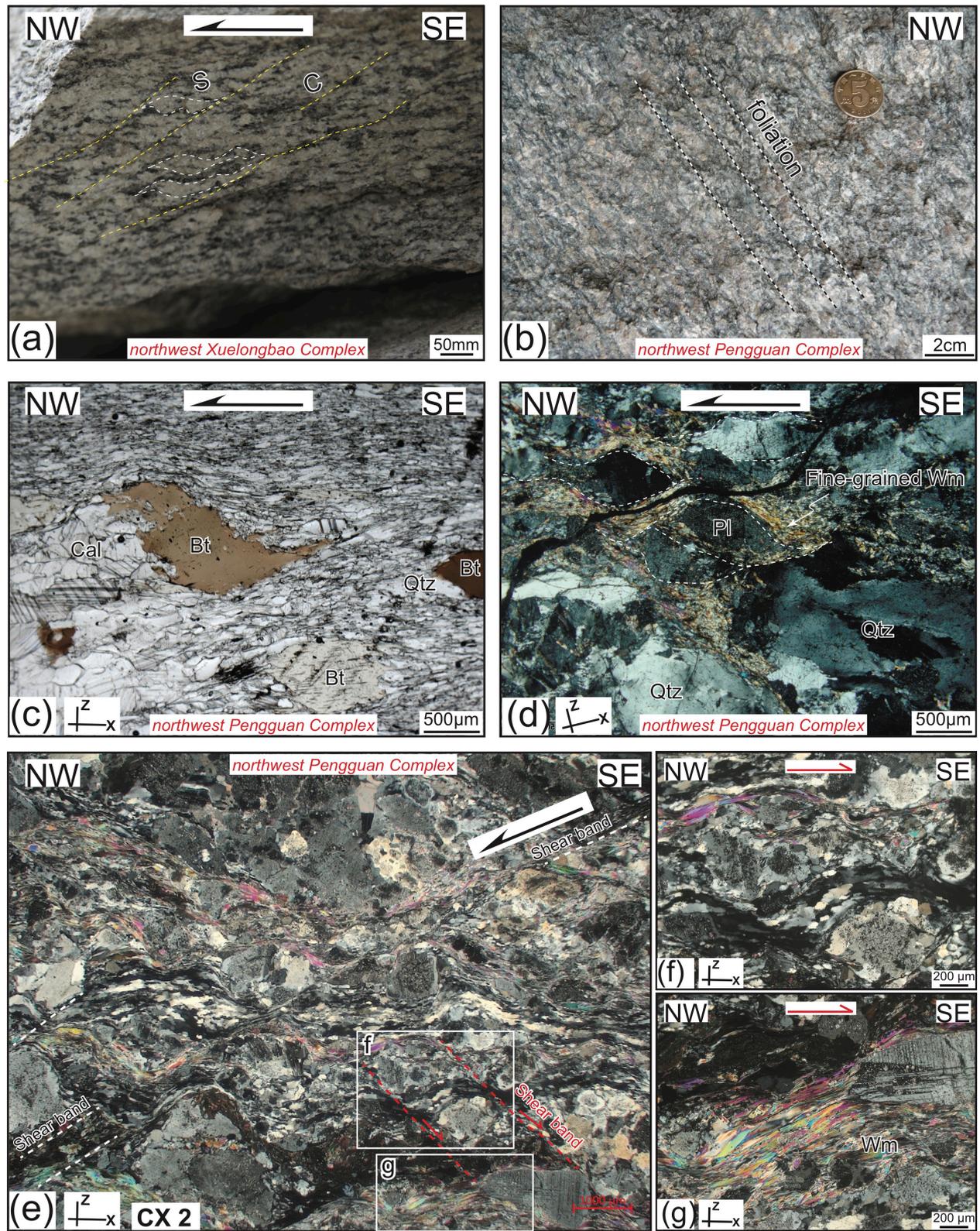
Figure 9

Figure 10

Northwestern Zone

(a) CX44 White mica — box heights are 2σ
Weighted mean age 224.1 ± 1.7 Ma
MSWD = 8.5, 81.66% of the ³⁹Ar
Total gas age 221.7 ± 3.5 Ma

(b) CX12A Fine-grained white mica — box heights are 2σ
146.5 ± 2.7 Ma
64.7 ± 0.3 Ma

(c) CX12B Fine-grained white mica — box heights are 2σ
119.0 ± 1.3 Ma
72.2 ± 1.4 Ma

Southeastern Zone --
Inner metamorphic core

(d) CX6A White mica — box heights are 2σ
Weighted mean age 124 ± 1.9 Ma
MSWD = 26, 49.57% of the ³⁹Ar
Total gas age 126.5 ± 1.6 Ma

(e) CX6B White mica — box heights are 2σ
Weighted mean age 126.3 ± 3.3 Ma
MSWD = 52, 52.42% of the ³⁹Ar
Total gas age 127.6 ± 1.7 Ma

(f) CX33 White mica — box heights are 2σ
Plateau age 148.2 ± 1.2 Ma
MSWD = 1.77, 60.1% of the ³⁹Ar
Total gas age 148.5 ± 1.2 Ma

(j) CX19A Fine-grained white mica — box heights are 2σ
133.7 ± 3.3 Ma
59.0 ± 0.3 Ma

Basement Complex

(g) CX2 White mica — box heights are 2σ
Weighted mean age 26.23 ± 0.99 Ma
MSWD = 16, 53.63% of the ³⁹Ar
Total gas age 29.5 ± 2.5 Ma

(h) CX25 White mica — box heights are 2σ
Weighted mean age 79.7 ± 2.7 Ma
MSWD = 62, 79.74% of the ³⁹Ar
Total gas age 82.6 ± 1.2 Ma

(i) CX18 Fine-grained white mica — box heights are 2σ
111.1 ± 0.2 Ma
50.0 ± 0.1 Ma

(k) CX19B Fine-grained white mica — box heights are 2σ
139.3 ± 1.1 Ma
58.4 ± 0.4 Ma

Axis labels: Age(Ma) vs Cumulative ³⁹Ar Percent

Figure 11

Figure 12

Figure 13

Figure 14

a — Pre-T$_2$ rifting

- "weak zone"
- Yangtze Block
- 20 km
- 10 km
- NW / SE

b — T$_3$ underthrusting

- Allochthonous sheet
- Autochthonous foreland basin
- décollement
- underthrust
- Yangtze Block
- Lower crust
- 20 km
- 10 km
- NW / SE

c — T$_3$ to J$_1$ heating and metamorphism

- décollement
- Yangtze Block
- Lower crust
- 20 km
- 10 km
- NW / SE

d — J$_3$ to K$_1$, K$_2$ to E$_1$ basement-slice episodic imbrication

- Inner meta-morphic core
- Allochthon
- Para-autochthon
- Autochthon
- LJG, MP, MCB, WMF, IFT/WLF, YBF, AGF
- Cretaceous conglomerate
- Yangtze Block
- décollement
- Lower crust
- 20 km
- 10 km
- NW / SE

Legend:
- ⟋ Pre T$_2$ normal fault
- ⟋ Reverse fault during T$_3$–aJ$_1$
- ⟋ Episodic and synchronous NW-normal faulting and SE-thrusting during J$_3$–K$_1$, K$_2$–E$_1$
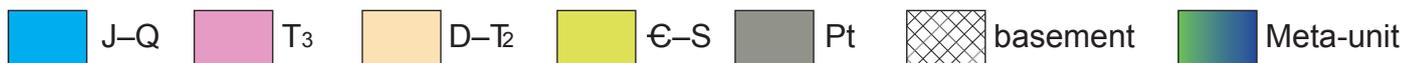
- J–Q
- T$_3$
- D–T$_2$
- Є–S
- Pt
- basement
- Meta-unit

Supplemental Material

Figure S1. (a) Reflection image show location of the crack in feldspar, same crack in lower middle of Figure 8e from the Mupi pluton. (b) Same crack in Figure a, cross-polarized light. (c) Back scattered electron image show points selected for energy–dispersive X-ray spectrometer measurement. (d and h) Energy–dispersive X-ray spectra of point 1 and point 6 in the crack show typical feature of quartz. (e–g) Energy dispersive X-ray spectra of point 2, point 3, and point 5 indicate component of feldspar with different Ca content.

Figures S2. Features of the samples selected for ^{40}Ar-^{39}Ar dating. Shear plane is defined by fine-grained white mica (c–d) or white mica (a–b, e–f, and g). (h) Field observation of sample CX6, where sigma-shaped quartz lens indicate a top-to-the-SE thrusting. Mineral abbreviations after Kretz (1983). CPL—cross-polarized light; PPL—plain-polarized light.

Figure S3. All samples show high radiogenic ^{40}Ar (Table S2) and almost all steps are clustered at the ^{39}Ar/^{40}Ar axis that do not define a real inverse isochron line. The initial ^{40}Ar/^{36}Ar ratio originate from the inverse isochron line is meaningless as well. Most of the step-ages calculated both by using initial ^{40}Ar/^{36} of 298.56 (Lee et al., 2006) and from the "inverse isochron", show nearly no differences (Table S2). Thus, the inverse isochron ages, though identical to their weighted mean ages or plateau ages, are meaningless and have not been discussed in the main text.

Table S1. Detailed SIMS U-Pb zircon results of sample CX48

**Table S2.** ^{40}Ar/^{39}Ar VG3600 Furnace Step-Heating analytical results

Figure S1
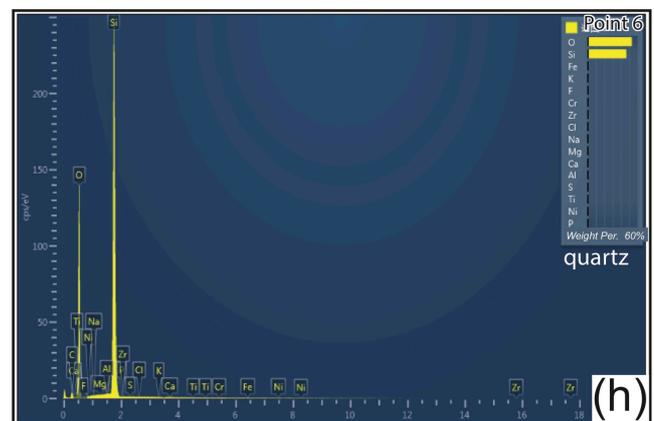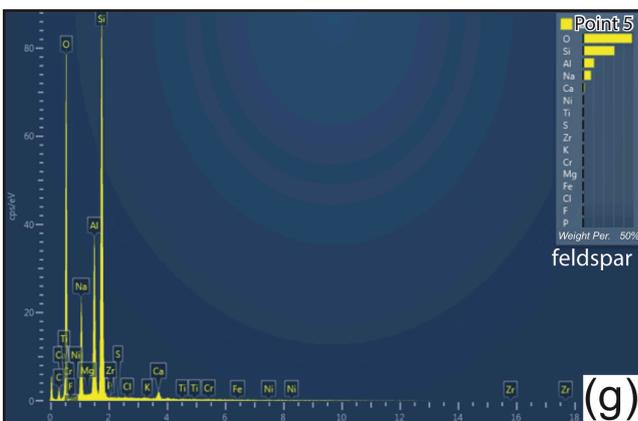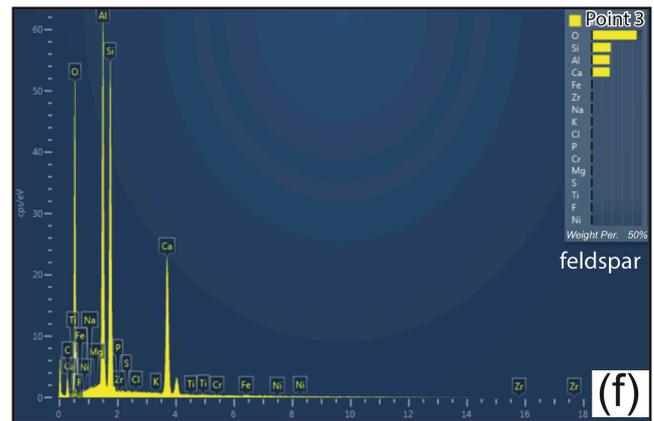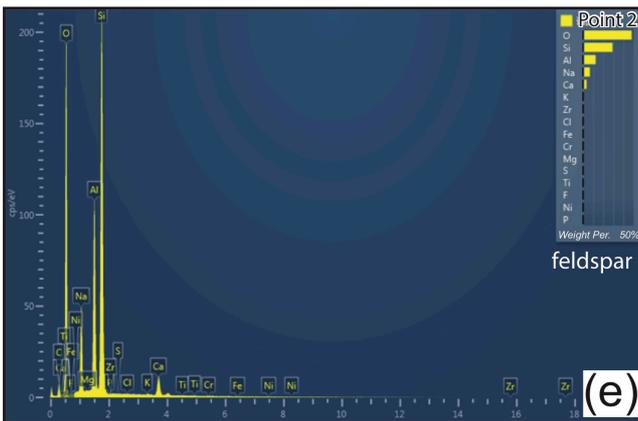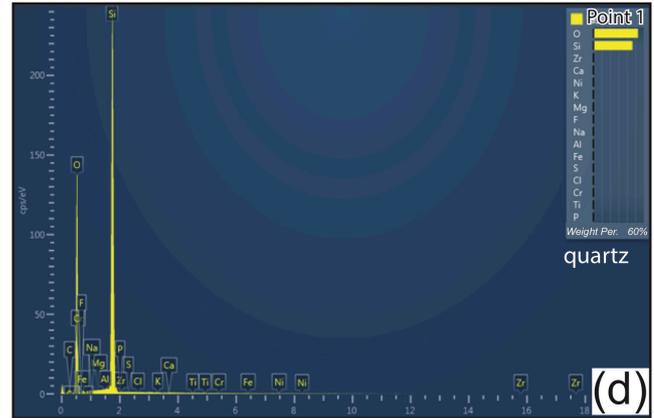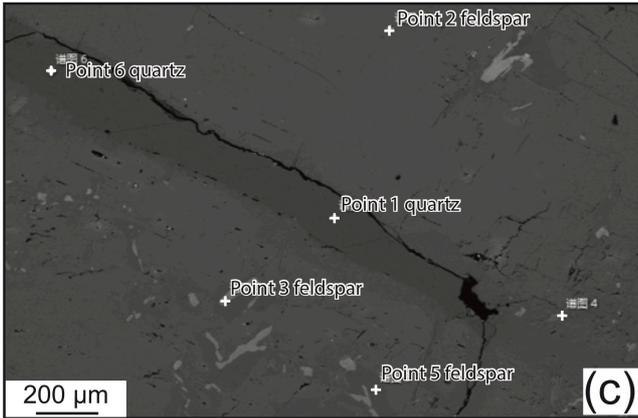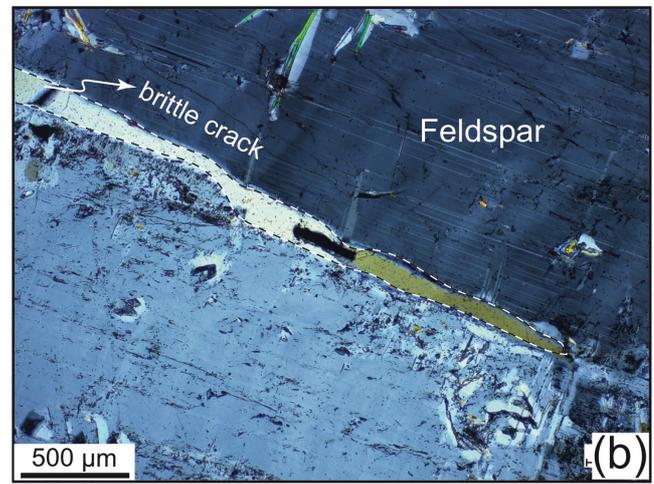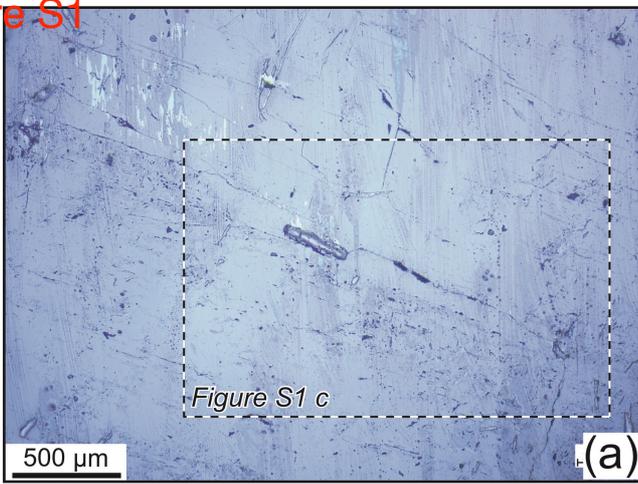
Figure S2
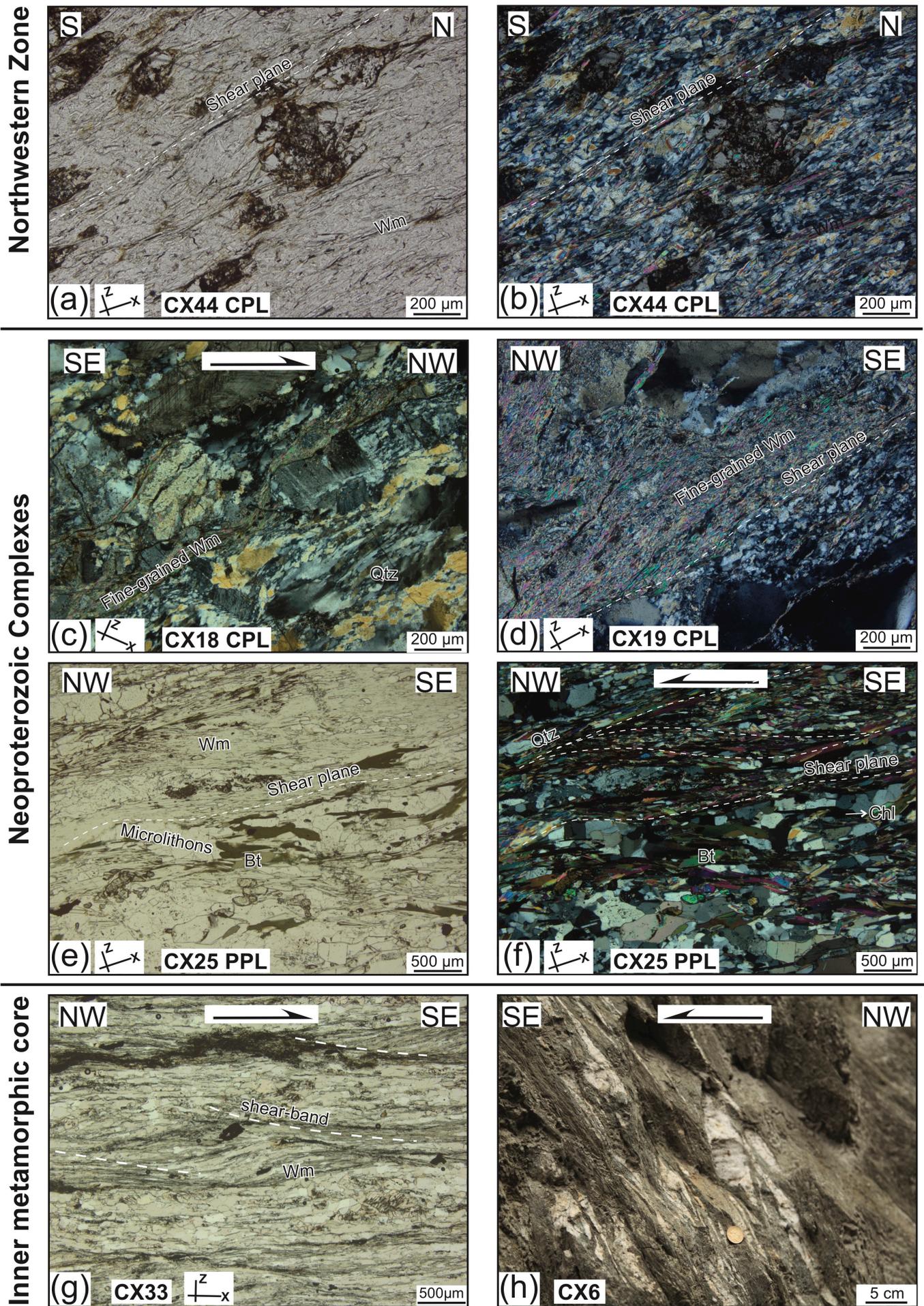
Figure S3

Northwestern Zone

(a) CX44 White mica
Inverse isochron age
223.9 ± 5.8 Ma
Initial $^{40}Ar/^{36}Ar$ = 289 ± 37

Southeastern Zone --
Inner metamorphic core

(b) CX6A White mica
Inverse isochron age
121.1 ± 6.8 Ma
Initial $^{40}Ar/^{36}Ar$ = 564 ± 170

(c) CX6B White mica
Inverse isochron age
125.7 ± 7.1 Ma
Initial $^{40}Ar/^{36}Ar$ = 900 ± 200

(d) CX33 White mica
Inverse isochron age
147.1 ± 1.5 Ma
Initial $^{40}Ar/^{36}Ar$ = 476.6 ± 169.7

Basement Complex

(e) CX2 White mica
Inverse isochron age
25.8 ± 3.6 Ma
Initial $^{40}Ar/^{36}Ar$ = 468 ±190

(f) CX25 White mica
Inverse isochron age
80.1 ± 6.5 Ma
Initial $^{40}Ar/^{36}Ar$ = 703 ± 200